

Contents lists available at ScienceDirect

International Journal of Mechanical Sciences

journal homepage: www.elsevier.com/locate/ijmecsci





Effects of microstructure and inherent stress on residual stress induced during powder bed fusion with roller burnishing

Sumair Sunny, Ritin Mathews, Haoliang Yu, Arif Malik *

Department of Mechanical Engineering, The University of Texas at Dallas, 800 W. Campbell Rd., Richardson, TX 75080, USA

ARTICLE INFO

Keywords: Hybrid additive manufacturing Powder bed fusion Roller burnishing Residual stress Microstructure modeling Finite element analysis

ABSTRACT

A hybrid metal-additive manufacturing (AM) process that combines laser-based powder bed fusion (PBF-LB) with interlayer burnishing is investigated using a comprehensive modeling framework to provide new insights into how the inhomogeneous microstructure and residual stress from the laser powder bed fusion process affect the induced residual stress field that evolves during interlayer burnishing. Researchers have recently studied changes in microstructure resulting from similar hybrid metal-additive processes, however, it was only hypothesized that the resulting microstructure has some influence on the induced residual stress. In addition, researchers have numerically investigated the influence of burnishing/rolling process parameters on induced stress but neglected the effects of microstructure, thereby making homogeneous, isotropic assumptions. Such practice inhibits the prediction of microstructure-driven anisotropy that can exist in the inhomogeneous fused layer. This paper parametrically examines the influence of microstructure modeling, inherent residual stress mapping, and environment temperature on the induced residual stress during the hybrid metal-additive process. The demonstrated modeling framework incorporates inherent residual stresses that emerge from the laser powder bed fusion process, as well as the predicted microstructure, in a subsequent burnishing simulation to elucidate their individual and combined influences on the burnishing-induced residual stress. Findings reveal that modeling an inhomogeneous PBF-LB microstructure introduces an anisotropic distribution of plastic strain and residual stress along the burnished surface; a periodicity in planar stress components along the treated surface coincides with the PBF-LB scan lines. Effects of inherent residual stress on the burnishinginduced residual stress is less significant, but nonetheless observable. Elevated temperatures not only reduce the magnitude of compressive residual stress induced but also result in less variation of residual stress component magnitudes predicted along scan lines and hatch spaces. The presented framework offers new insights into the decoupled influences of microstructure and PBF-LB residual stress on burnishing-induced stresses that are not distinguishable via experimental techniques. However, trends in averaged residual stress through the depth of the specimen, as well as surface hardness magnitudes after burnishing show good agreements, respectively, with X-ray diffraction and microindentation measurements documented in the literature.

1. Introduction

The state of residual stress (RS) is an important criterion when assessing the surface integrity of an engineered component. A high compressive residual stress (CRS) and surface hardness can substantially improve the fatigue life and wear resistance of manufactured parts [1,2]. Laser-based powder bed fusion (PBF-LB) methods such as selective laser melting (SLM) [3,4], give rise to undesired tensile residual stress (TRS). TRS can lead to distortion, delamination and even part failure during the metal-additive build process [5]. In addition, warping and cracking are commonly seen setbacks of SLM. Numerous methods have been applied to mitigate TRS and/or promote CRS, however, each approach has its own challenges. Heat treatment can be used to

alleviate TRS, however, as noted by Wang et al. [6] who examined the effects of heat treatment on directed energy deposition Inconel 625, heat treatment can cause changes in the microstructure, potentially changing strain-free lattice spacing, which affects neutron diffraction measurements of lattice strain, leading to erroneous measurements of residual stress and strain. Kalentics et al. [7] discussed the use of in-situ laser shock peening to induce CRS in an SS 316L specimen, thereby decreasing crack propagation rates on the treated surface, reducing stress intensity factors, enhancing fatigue crack closure phenomenon, and increasing the threshold stress for crack propagation. Their approach, however, was pseudo-hybrid, considering that the SLM part had to be removed from the printer and placed into another machine

E-mail address: Arif.Malik@utdallas.edu (A. Malik).

Corresponding author.

for the subsequent laser shock peening treatment, after which it was returned for the printing of another 'n' layers [8]. Such a practice makes it difficult (if not impractical) to guarantee geometric precision, especially for parts with intricate features. Meyer and Wielki [9] used a similar pseudo-hybrid approach that combined SLM with interlayer rolling for SS 316L and observed, via X-ray diffraction (XRD), high compressive residual stresses imparted near the surface along with dislocation slip, twinning and strain hardening at a greater depth from the treated surface. Note that removing and re-integrating the part in the printer environment can affect the thermal history governed microstructure [10]. From work by Courbon et al. [11], who examined surface integrity of turning and ball-burnished, cold-sprayed and laser cladded 17-4 PH steel, it is suggested that the inherent microstructure of the deposited material may influence, to some degree, the induced RS during the burnishing process. Hybrid manufacturing processes combining wire arc additive manufacturing (WAAM) with insitu rolling have been discussed by Colegrove et al. [12], and Donoghue et al. [13]. While the hybrid process successfully transformed TRS to CRS, electron backscatter diffraction (EBSD) imaging confirmed the presence of an inhomogeneous microstructure with epitaxial grain growth resulting from WAAM. Donoghue et al. noted that the hybrid process disrupted the formation of coarse, columnar, epitaxial grains that formed with the continuous deposition of numerous layers. A summary of the state of the art in experiments and numerical work combining burnishing and rolling/micro-rolling and metal additive manufacturing is presented in Table 1. Note, the context in which burnishing, rolling/micro-rolling have been implemented, as discussed in Table 1, is exactly the same; the objective of the research was to improve aspects of surface integrity, i.e., induce CRS, reduce surface roughness, and improve surface hardness.

From Table 1 it is evident that a hybrid metal-additive process, when incorporating burnishing (including UVAB) or rolling, can transform undesired built-up TRS that arises during the additive process to CRS, thereby improving the fatigue life of additively built parts. Nevertheless, certain aspects of the hybrid manufacturing process model require further investigation:

- The degree to which the inherent residual stress field from the PBF-LB process influences the burnishing/rolling induced stress field needs to be clarified.
- Microstructural inhomogeneity that arises from the PBF-LB process can result in an anisotropic response within the fused layer [23], hence, the influence (if any) of the inherent microstructure on the induced residual stress needs to be examined.
- 3. An elevated temperature in the hybrid manufacturing environment may be conducive to formability of the material, however, it may adversely affect the magnitude of CRS induced. Thus, the influence of environment temperature on burnishing/rolling induced CRS needs to be assessed.

Given that the combined effect of inhomogeneous microstructure, PBF-LB inherent RS, and burnishing temperature has not been investigated in the past, the three factors serve as motivation for the modeling framework presented in this paper that proposes a hybrid metaladditive process combining SLM with interlayer burnishing, as illustrated in Fig. 1. Note that the presented framework offers new insights into the decoupled influences of microstructure and SLM residual stress on burnishing-induced stresses that are not distinguishable via experimental techniques. In the demonstrated model, a 400 W Yb-fiber laser will fuse a deposited layer of Inconel 625 powder. Upon the completion of the laser scans for the layer, a roller-burnishing operation will commence to transform TRS to CRS within the fused layer. The nickel superalloy is used herein considering its wide array of applications across numerous industries including the aerospace, chemical, petrochemical, marine, and nuclear, given its processability, weldability, and high temperature corrosion resistance [24-27]. The alloy is especially resistant to crevice and pitting corrosion [28]. This work

seeks to elucidate the influence of microstructure modeling, inherent residual stress, and environment temperature on the induced state of stress that results from the hybrid metal-additive process. Accordingly, Section 2 of this paper describes a physics-based thermomechanical finite element (FE) model by which the thermal and residual stress histories from the SLM process are predicted. Furthermore, the transient thermal history is implemented in a microstructure prediction model from which a representative volume element is generated for use in the subsequent interlayer burnishing simulation. Section 3 describes a thermomechanical FE model for the burnishing process which maps the inherent residual stress predicted from the SLM simulation as an initial state. In addition, the material constitutive modeling used to implement inhomogeneity into the representative volume element is discussed. Trends in the inherent residual stress field arising from the SLM process, as well as, trends in the burnishing-induced residual stress field are presented in Section 4, along with brief discussions on predicted hardness and equivalent plastic strain across the burnished surface. Finally, a summary of the key findings from the parametric studies performed in this work is presented in Section 5.

2. Prediction of laser powder bed fusion residual stress and microstructure with finite element mapping

A Lagrangian FE model is used to simulate the PBF-LB process, wherein a single layer of Inconel 625 is melted (or fused) atop an Inconel 625 substrate, as illustrated in Fig. 2. Linear hexahedral coupled temperature-displacement elements are used to discretize powder and solid continua in the numerical model. Since only a single powder layer is being modeled herein, discussion on approaches such as the quiet elements and/or inactive elements can be omitted. These methods are required to model subsequent powder layer depositions [29,30], as well as keyhole phenomenon and lack of fusion porosities [31-33]. Referring to Fig. 2, a structured 25 µm cubic element mesh is used to discretize the 5 mm × 4 mm area of powder continua to be scanned, while the surrounding powder and solid substrate employs a relatively coarser meshing scheme. This is done to reduce the computational expense of the simulation; Since the 2 mm \times 0.5 mm \times 0.2 mm subset, within which RS will be examined, is spatially located within the scanned area, any loss of accuracy associated to the coarsely meshed regions will not affect the RS field being probed. Python scripting along with a DFLUX Fortran user-subroutine is used to sequence and implement the dynamic heat source that traverses the laser scan lines in the model. Solutions for the thermomechanical model are computed using the implicit solver of Abaqus v6.14. Physics-based modeling of the PBF-LB process is discussed next, following a brief overview of the infrared thermography experiments being emulated.

2.1. Overview of infrared thermography to capture melt pool dynamics

Thermomechanical modeling demonstrated in this work, for PBF-LB with Inconel 625, emulates an infrared thermography experiment conducted at the National Institute of Standards and Technology, documented by [34-37]. A short-wave infrared camera (IRC912) was retrofitted to the window of an EOS M270 printer [38,39]. High-speed (1800 fps) thermographic imaging was employed to capture measurements of the thermal field surrounding a dynamic melt pool (MP) during single and multiple scans of a "hand-spread" layer of Inconel 625 powder over a substrate of the same material, with dimensions of 25.4 mm × 25.4 mm × 3.2 mm, as illustrated in Fig. 2. Laser power was parametrically varied between 49 to 195 W, while scan speed was from 200 to 800 mm s⁻¹. A discontinuity in the radiant temperature gradient along a path moving radially away from the center of the MP was found to be indicative of the solidus-liquidus transition, thereby identifying the MP boundary (or isotherm). Calibration of the dynamic MP geometry in the thermal model, discussed next, is based on the PBF-LB thermography dataset for 195 W at 800 mm s⁻¹ [40].

Table 1
Summary of the state of the art in experiments and numerical work combining burnishing and rolling/micro-rolling and metal additive manufacturing.

| Summary of the state | of the art in experiments and | numerical work combining burnishing and rolling/micro-rolling and metal additive manufacturing. |
|---------------------------------------|---|--|
| Author (Year) | Process Investigated and Materials | Summary of Key Details, Findings and Assumptions Relevant to the Present Work |
| Colegrove et al. (2013) [12] | Hybrid mfg. process: wire arc additive mfg. (WAAM) with in-situ rolling; Structural steel (grade S355JR-AR) | Experimentally studied the trends in microstructure and RS of structural steel plates deposited that result from the hybrid process of WAAM with in-situ rolling. Results revealed longitudinal-bowing distortion was significantly reduced by rolling. Different roller profiles influenced the deformation and RS fields. Longitudinal and transverse stress components became compressive in nature. Heat treatment when the subsequent layer was deposited resulted in grain refinement. Grain refinement was enhanced by plastic deformation induced by intralayer rolling. |
| Zhou et al. (2016) [14] | Prediction of microstructure from hybrid wire deposition and micro-rolling process; SS 316L | Developed a computational framework to predict SS 316L microstructure that resulted from a hybrid gas metal arc welding deposition and micro-rolling process. Thermal fields from the FE simulation were used to predict nucleation and grain growth via cellular automata. Dynamic recrystallization (DRX) was used to predict effects of micro-rolling on grain morphology by using a strain field from the FE model to compute dislocation density at every increment of time. The roller would follow the wire bead immediately after deposition, suggesting that hot rolling was executed, which may have a dominant effect on microstructure. Equiaxed microstructure was predicted in the DRX regions. |
| Donoghue et al. (2016) [13] | Hybrid mfg. process: WAAM with in-situ rolling; Ti-6Al-4V | Experimentally investigated β-grain refinement and texture modification during the hybrid process of WAAM combined with intralayer rolling. EBSD imaging of the WAAM structure revealed coarse columnar β-grain formation with epitaxial growth resulting in an inhomogeneous microstructure. Introduction of rolling spurred a more homogeneous microstructure with more refined β-grains and weakened β- and β-grain textures. Homogeneity of the refined β-grains was observed to improve with greater rolling deformation. A study with similar findings was reported by [15], which additionally discusses how peak TRS was significantly reduced at the interface with the baseplate, and that rolling induced significant CRS near the top of the deposit which then reversed, at the surface, becoming slightly tensile in character [16]. The hybrid process disrupts the formation of coarse, columnar, epitaxial grains that form with the continuous deposition of numerous layers. |
| Fu et al. (2017) [17] | Hybrid mfg. process: WAAM with rolling; Bainitic steel | Experimentally investigated the influence on yield strength and impact toughness in the hybrid mfg. process. Yield strength showed insignificant increase. Impact toughness increased approximately 3 to 4-fold. Anisotropy in WAAM samples was eliminated by the hybrid process, which resulted in an average grain size of 7 µm. |
| Wang et al. (2017) [18] | Ultrasonic surface-rolling process (USRP) of SLM part; Ti-6Al-4V | Conducted experiments to study influence of USRP on microstructure and wear behavior. Used a spherical roller (14 mm diameter), 30 kHz vibration frequency, 8 µm amplitude, 1 kN load and a linear travel speed of 1 m min⁻¹. Severe work hardening was observed in the densified layer, attributed to grain refinement, formation of new dislocation boundaries and deformation twins. 14.1% increment in Vickers hardness at the surface was observed, which decreased gradually through the depth. USRP improved the hardness and shear resistance whilst impeding the initiation of interlayer delamination. |
| Breidenstein et al. (2018) [19] | Face milling and deep rolling of SLM parts; H13 tool steel | Experimentally investigated changes in surface and subsurface properties including roughness, hardness and RS. Parametrically varied build platform temperature from 473 to 873 K to examine the influence of platform temperature on RS and hardness. As-built SLM samples exhibited TRS, however higher temperatures resulted in relatively reduced TRS. Following deep rolling operations, these stresses changed to compressive with a smaller roller diameter resulting in greater CRS. Hardness was found to vary based on the SLM platform temperature; The lower SLM platform temperatures, 473 to 673 K, resulted in relatively higher hardness post machining in comparison to 873 K. Milling when performed post SLM, was found to moderately increase the TRS such that under certain conditions CRS would not be achieved when subsequent deep rolling was performed. |
| Meyer and Wielki (2019) [9] | SLM with interlayer deep rolling; SS 316L | Experimentally studied the effects on surface roughness, porosity changes, dislocation slip and twinning effects. The AM part was removed from the 3D printer for the rolling process and subsequently returned for deposition and melting of the subsequent layer. Note, this can potentially affect the thermal history and geometric accuracy. EBSD imaging revealed recrystallization near the heat affected zones (HAZ) from subsequent layer depositions, with dislocation slip and twinning observed in the strain-hardened layers, at a greater depth from the surface. XRD revealed high compressive stresses (500 to 600 MPa) at the surface post rolling. Vickers microhardness tests revealed hardness in the top layers (approximately 230 µm of depth) appeared to reduce due to the thermal effects during the subsequent SLM cycle; Post rolling, hardness was measured to be in the range of 350 to 400 HV0.5, however post SLM of the subsequent powder layer, this range reduced to 225 to 300 HV0.5. |
| Teramachi and Yan (2019) [20] | Ultrasonic vibration-assisted burnishing (UVAB) of AM parts; ALSi10Mg | • Experimented with UVAB to improve the surface integrity of AM AlSi10Mg components. • Used a ceramic ball burnishing head with a 100 m s ⁻¹ feed rate, at a 27 kHz frequency and 0.8 μ m vibration amplitude on the 30 μ m surface layer. • Void closure, assessed via X-ray micro-computed tomography revealed up to 96% improvement in the first 200 μ m of depth from the treated surface and as much as ~90% even at depths of 1.4 mm. • Vickers hardness tests revealed ~24% increase in hardness as a result of the UVAB treatment. • The ultrasonic vibrations helped reduce the burnishing force required and tool wear was found to be insignificant. |
| Ituarte et al. (2020) [21] | UVAB of AM parts; 18Ni maraging steel | • Performed experiments to examine the effects of UVAB, including changes in surface roughness, microhardness and near-surface RS. • Surface hardness was found to increase from $\sim \! 505$ to $\sim \! 567$ HV1. • Average surface roughness (Ra) reduced from 6.24 μm to as little as 0.14 μm . • XRD results revealed that high CRS was induced by UVAB. |

(continued on next page)

Table 1 (continued).

| Author (Year) | Process Investigated and Materials | Summary of Key Details, Findings and Assumptions Relevant to the Present Work |
|-------------------------------|--|--|
| Courbon et al. (2019) [11] | Turning and ball-burnishing, cold sprayed and laser cladded steel; 17-4 PH stainless steel | Experimentally examined surface integrity of cold sprayed and laser cladded stainless steel deposits after turning and ball-burnishing. High-resolution scanning electron microscopy revealed that both turning and ball-burnishing resulted in 5 to 10 μm of deformation below the treated surface. This led to a slight increase in microhardness near the surface. Turning resulted in near-surface TRS in both cold spray and laser cladding operations, followed by a CRS deeper into the specimens. Ball-burnishing improved surface integrity of both deposits by transforming TRS to CRS up to a depth of 300 μm. It was, however, noticed that the magnitude of CRS induced was nearly 5 times greater for laser cladded deposit (-1 GPa) in comparison to the cold sprayed one (-200 MPa), suggesting that microstructure of the deposited material may have some effect of the RS distribution. |
| Rotella et al. (2020) [22] | Roller-burnishing of SLM specimen; GP1 stainless steel | Experimentally investigated the surface integrity in terms of roughness, hardness, microstructure and RS. Burnishing was conducted with a 5 and 10 mm diameter roller, at 50, 150, and 200 m min⁻¹, with feed rates of 0.05 to 0.1 mm rev⁻¹. The burnishing forces used were 1000, 1500 and 2000 N. Average surface roughness (Ra) reduced from 11 μm (as-built) to between 0.2 μm and 0.4 μm after treatment. Pore closure effects and increased surface hardness were documented. The cold process did not modify the microstructure and a deep CRS was induced. The burnishing process was found to improve fatigue performance, particularly with an increase in rolling force. |

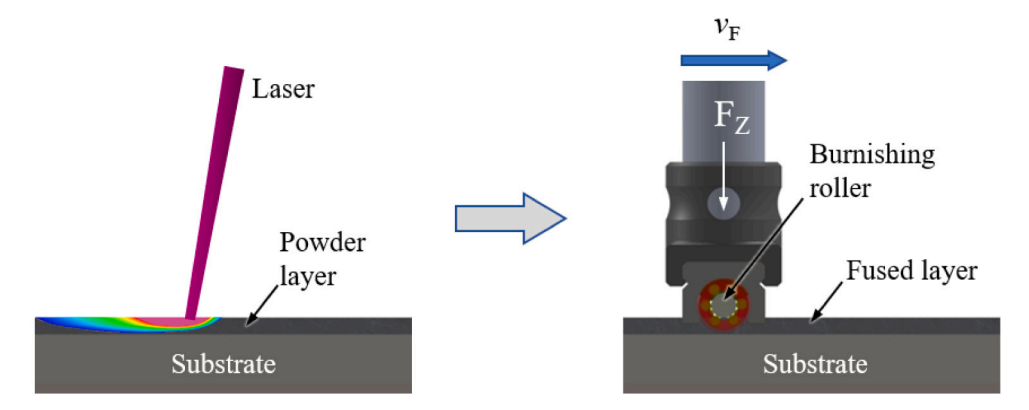


Fig. 1. Illustration of the hybrid additive manufacturing process featuring laser powder bed fusion with interlayer burnishing. (Left) The laser scanning of the deposited powder layer thereby fusing it. (Right) Subsequent interlayer roller-burnishing of the fused layer.

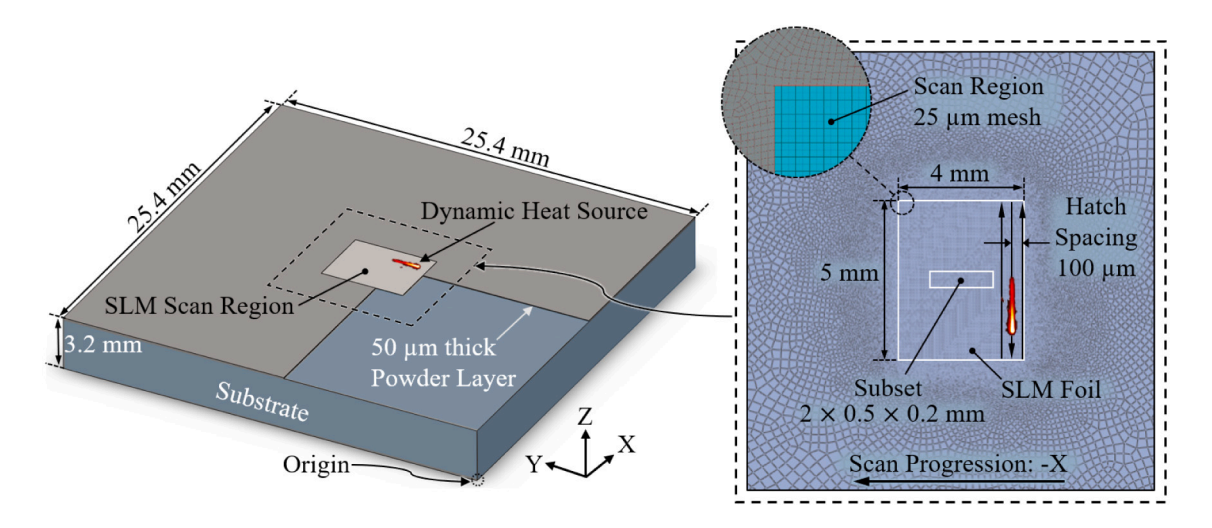


Fig. 2. Schematic of the selective laser melting powder bed fusion finite element model to emulate an Inconel 625 infrared thermography experiment performed at the National Institute of Standards and Technology [34].

2.2. Thermal model for laser powder bed fusion

The 3D heat-energy balance relation [41], governing the spatial and temporal distribution of temperature, T, in the FE model is given by Eq. (1). This relation is applicable for both powder and solid (or fused)

continua in PBF-LB process. Note that similar modeling approaches have also been adopted by other researchers who investigated powder bed fusion and directed energy deposition processes [42–45].

$$\nabla \cdot (\mathbf{k}\nabla \mathbf{T}) + \mathbf{q} = c_{\mathbf{v}}\rho \frac{\partial \mathbf{T}}{\partial t}, \quad \text{for} \quad t \ge 0$$
 (1)

In Eq. (1), the thermal conductivity, k, specific heat (constant volume), c_v , and density, ρ , are temperature dependent terms. Temperature dependent material properties for Inconel 625 used in the demonstrated work are referenced from [6,46]. As discussed by Foroozmehr et al. [47], the density and thermal conductivity of powder continua are empirically considered to be 40% and 1%, respectively, of those of the solid continua. Before the laser scans commence, the substrate is modeled with the material properties of solid continua, while the powder layer is modeled with those of the powder continua. During the PBF-LB simulation, as the temperature at any given location exceeds the melting temperature, T_m, of Inconel 625 (1898 K), the temperature dependent curves for the respective material properties are switched to those of the solid, given that the location will form part of the solid continua upon cooling. The dynamic laser heat source, q, is mathematically described by Goldak et al.'s double ellipsoid model given by Eq. (2).

$$\mathbf{q} = \begin{cases} \frac{6\sqrt{3}f_{\mathbf{f}}PA}{abc_{\mathbf{f}}\pi\sqrt{\pi}} e^{-3\frac{X^{2}}{a^{2}}} e^{-3\frac{Z^{2}}{b^{2}}} e^{-3\frac{(Y+vt)^{2}}{c_{\mathbf{f}}^{2}}}, & Y \ge Y_{i} \\ \frac{6\sqrt{3}f_{\mathbf{f}}PA}{abc_{\mathbf{f}}\pi\sqrt{\pi}} e^{-3\frac{X^{2}}{a^{2}}} e^{-3\frac{Z^{2}}{b^{2}}} e^{-3\frac{(Y+vt)^{2}}{c_{\mathbf{f}}^{2}}}, & Y < Y_{i} \end{cases}$$
 for $t > 0$ (2)

Heat source model parameters, illustrated in Fig. 3, need to be calibrated such that the simulated MP dimensions, discussed later in Section 2.4, can closely replicate those measured in the thermography dataset, employing the same power, P, and scan speed, v. The calibrated parameters governing the geometry of the dynamic heat source for the demonstrated work are listed in Table 2.

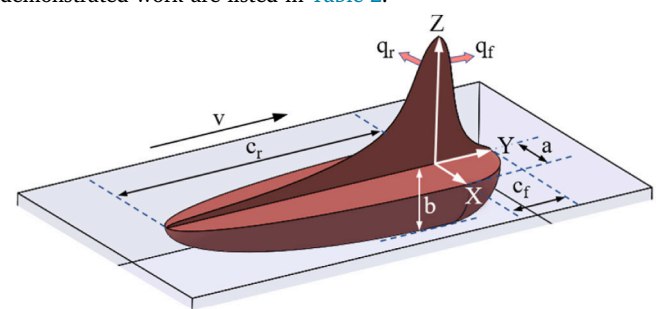


Fig. 3. Geometric parameters governing the shape of the dynamic heat source.

Double ellipsoid heat source model parameters.

| Parameter | Values |
|----------------|--------|
| a | 182 μm |
| b | 181 μm |
| c_f | 180 μm |
| c _r | 540 μm |
| f_f | 1.4 |
| f _r | 0.6 |

As reported by [48], elevated environment temperature via preheating can reduce or even mitigate the TRS developed in the specimen. While this is desirable, the goal of the PBF-LB model in this work is to reveal significant TRS in the fused layer, so as to predict the extent to which this TRS can be reduced during the interlayer burnishing process that follows. Hence as an initial condition, the ambient (or sink) temperature, $T_{\rm amb}$, in the PBF-LB model, applied to the substrate and deposited powder, is assigned as approximately room temperature (296 K) per Eq. (3), i.e., no preheating is considered.

$$T(\mathbf{X},0) = T_{amb} \tag{3}$$

During the PBF-LB process, as heat is added to the system, modes of heat transfer and loss simulated are via conduction to surrounding solid and powder continua, as well as convection and radiation from all the free surfaces, Γ , as described by Eq. (4).

$$-k\nabla T \cdot \hat{\mathbf{n}} + h\left(T - T_0\right) + \Psi \epsilon \left(T^4 - T_0^4\right) = 0, \text{ on surface } \Gamma$$
 (4)

In Eq. (4), Ψ is the Stefan–Boltzmann constant (5.6703 \times 10⁻⁸ W m⁻² K⁻⁴). Other constants such as emissivity, ϵ , convective heat transfer coefficient, h, and absorptivity, Λ (Ref. Eq. (2)), once calibrated using the thermography dataset, can be used for different power and scan speed combinations. The PBF-LB process parameters and calibration constants used in the demonstrated work are listed in Table 3.

Table 3
PBF-LB process parameters and calibration constants.

| Parameter | Values | |
|-----------------|--------------------------------------|--|
| P | 195 W | |
| v | 800 mm s ⁻¹ | |
| Scan pattern | Bi-directional | |
| Layer thickness | 50 μm | |
| Hatch spacing | 100 μm | |
| Λ | 0.48 | |
| ϵ | 0.65 | |
| h | 10 W m ⁻² K ⁻¹ | |

2.3. Mechanical model for laser powder bed fusion

Thermo-fluid modeling is not considered in this work, hence, minor deformation during the multi-phase transient melting process that stems from inertia, gravitational effects and viscous behavior of the MP are neglected. Such deformation, being relatively small in comparison to the thermally induced distortion computed by the FE model, cannot be captured in detail with the 25 μ m mesh resolution used for the scanned region. Typically, a discrete element method to model the powder particles (with mesh sizes as small as 1 μ m) employing volume of fluid method for tracking free surfaces, is used for capturing thermofluid effects [49,50]. This can reduce the stable time increment to the order of 1 ns [51], making the simulation very computationally intensive, and unnecessary to illustrate the findings in the demonstrated work. Hence, for the PBF-LB process being modeled, a quasi-static stress equilibrium relation given in Eq. (5), is used in conjunction with Eqs. (1)–(4).

$$\nabla \cdot \sigma = 0 \tag{5}$$

In Eq. (5), σ is the Cauchy stress tensor for which the thermal-elastic-plastic constitutive relation is given by Eqs. (6)–(10), where C is the 4th order homogeneous isotropic elasticity tensor and ϵ , $\epsilon_{\rm E}$, $\epsilon_{\rm P}$, and $\epsilon_{\rm Th}$ are the total, elastic, plastic, and thermal strain tensors, respectively. The term α represents the temperature dependent thermal expansion coefficient and I is a 3 \times 3 identity matrix.

$$\sigma_{n+1} = \sigma_n + \Delta \sigma \tag{6}$$

$$\Delta \sigma = C(\Delta \epsilon_{\rm E}) \tag{7}$$

$$\Delta \epsilon_{\rm E} = \Delta \epsilon - \Delta \epsilon_{\rm p} - \Delta \epsilon_{\rm Th} \tag{8}$$

$$\Delta \epsilon_{\mathbf{p}} = \dot{\epsilon_{\mathbf{p}}} \Delta t \tag{9}$$

$$\varepsilon_{\rm Th} = \alpha \Delta T[I] \tag{10}$$

Displacement boundary conditions are imposed on the lower surface of the substrate (see Fig. 2) as described by Eq. (11).

$$U_X = U_Y = U_Z = 0$$
, on surface $Z = 0$ (11)

Equations 1–11 represent the thermomechanical model that enables prediction of RS during the PBF-LB process. As discussed earlier, a set of experimentally determined temperature-dependent material properties, including Young's modulus, k, α , c $_{\rm v}$, and ρ for IN625, adopted from [6, 44,46,52] are tabulated into the model. Denlinger et al. [44], who used the same thermo-elastic–plastic modeling approach, compared the predicted distortion with that measured using a differential variable

reluctance transducer. They also compared the predicted thermal history with that measured using a K-type thermocouple, and obtained good agreement for both comparisons. Referring to Eqs. (8)–(10), note that excess thermal expansion can drive strain beyond the yield strain limit, introducing plastic strains and elastic–plastic material behavior with strain hardening. The thermal history predicted by the calibrated PBF-LB model is used as input for the microstructure prediction tool, described next.

2.4. Microstructure prediction and computationally efficient FE mapping

The Dynamic Kinetic Monte Carlo (DKMC) method, introduced by Sunny et al. [53] is implemented to predict a three-dimensional microstructure, within the subset, based on the thermal history of each node obtained from the PBF-LB simulation. Prior to this, however, the thermal history from the FE simulation is calibrated using the infrared thermography to identify appropriate heat source model parameters and the convective heat transfer coefficient. Once calibrated, this same FE model formulation can be applied with any geometry (for the same material and similar PBF-LB process parameters). Subsequently, the DKMC model is executed using the spatial and temporally varying MP and HAZ extracted from the FE simulation's thermal history. DKMC adopts its curvature-driven grain growth and nucleation models directly from the modified KMC Potts model introduced by Rodgers et al. [54]. A key strength of the DKMC method over the KMC method is that it is not limited to modeling microstructure that results only from steady-state MP and HAZ behavior, and can additionally predict microstructure resulting from transient variations in MP and HAZ dimensions. The underlying KMC Potts model features an on-lattice technique wherein stochastic grain growth/evolution occurs by Monte Carlo switches in "spin numbers" (or unique integer identifiers) for lattice sites. Contiguous lattice sites with differences in their spin allow for identification of the grain boundaries. During the simulation the total system energy increases with the addition of boundaries via nucleation. Conversely, the merging of boundaries via grain growth effectively reduces (or minimizes) the system energy. The randomly generated and assigned spin numbers that facilitate grain growth are therefore accepted by the algorithm, while spin number changes that increase system energy are probabilistically accepted according to the metropolis algorithm [55]. Thus, both nucleation and subsequent grain growth can occur within the MP region, albeit due to size differences between the MP and HAZ the amount of post-nucleation grain growth within the MP region is relatively limited compared to that observed within the HAZ for a given duration of time. Grain boundary mobility in the HAZ is governed by an Arrhenius relationship [56] with localized temperature. Near the solidification front, the mobility is higher, and as the temperature drops (i.e., towards the HAZ boundaries) the mobility

decreases. For more specific details on the underlying Monte Carlo method formulation, as well as a comparison of its benefits and challenges with alternative methods such as Cellular Automata FE [57,58] and Cellular Automata-Lattice Boltzmann [59] models, the reader is referred to [54]. Challenges such as the inability of the Potts model to incorporate crystal orientation and its corresponding anisotropic effects persist in the DKMC method and offer avenues for future improvement of the model.

While electron backscatter diffraction (EBSD) imaging can also be used to predict microstructure, the data obtained is 2D, and suitable assumptions have to be made about the out-of-plane characteristics of the microstructure [23]. In comparison, the DKMC method offers a 3D microstructure prediction considering effects of interlayer and intralayer heat accumulation. While existing KMC-based methods are limited to face centered cubic and body centered cubic crystal structures [60], Inconel 625 exhibits a face centered cubic lattice [61,62], hence use of DKMC is appropriate.

In the demonstrated work, the DKMC model uses a 'frame-by-frame' thermal history for every node, obtained from the PBF-LB simulation as seen in Fig. 4(a). Equations 12 and 13 define a set of eight time-dependent parameters, $\lambda_{\rm j}$, illustrated in Fig. 4(b), controlling the transient variations in dimensions of the MP and HAZ for the j'th frame of time, t. The isotherm boundaries for the MP and HAZ are based on melting temperature, $T_{\rm m}$, and recrystallization, $T_{\rm R}$ as determined by [53].

$$\begin{cases} \text{MP} \\ \text{HAZ} \end{cases}_{j} = \begin{cases} \mathbf{X}, & \forall & T(\mathbf{X}) \ge T_{\text{m}} & \text{for } t = t_{j} \\ \mathbf{X}, & \forall & T_{\text{R}} < T(\mathbf{X}) < T_{\text{m}} & \text{for } t = t_{j} \end{cases}$$
 (12)

$$\lambda_{j} = \begin{cases} MP & Cap \\ MP & Tail \\ MP & Width \\ MP & Depth \\ HAZ & Cap \\ HAZ & Tail \\ HAZ & Width \\ HAZ & Depth \end{cases} \quad \subset \quad \begin{cases} MP \\ HAZ \end{cases}^{T}_{j}$$

$$(13)$$

Once executed, the DKMC model predicts the shape and spatial location of individual grains within the volumetric domain of the subset. The calibration constants for the PBF-LB process influence the predicted microstructure and can be verified using EBSD or scanning electron microscopy images from an AM build featuring the same material and process parameters. For brevity, such a comparison is not discussed in detail herein, however, the reader is referred to [23] to see an example of the same.

In this work, approximately 1108 grains are predicted as shown in Fig. 5a (*Top*). The microstructure is depicted using different colors

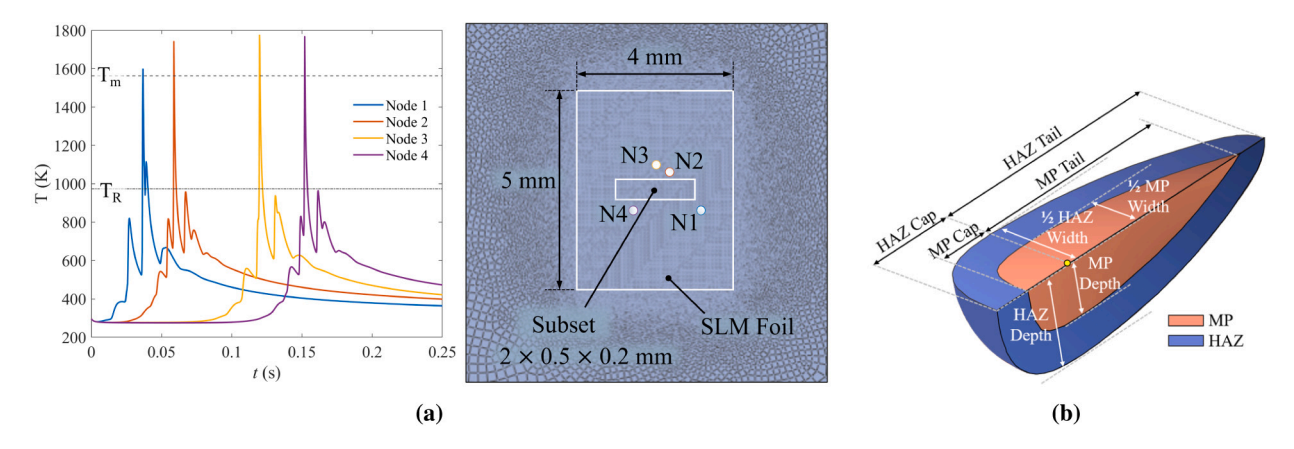


Fig. 4. (a) Thermal histories of four arbitrary nodes from the top surface of the scanned region in the PBF-LB simulation (Ref. Fig. 2). Coordinates of these nodes are: Node 1 (14.15, 11, 3.2 mm), Node 2 (13.75, 13.3, 3.2 mm), Node 3 (12.75, 14.45, 3.2 mm), and Node 4 (12.25, 11.65, 3.2 mm). (b) Schematic of the melt pool and heat affected zone geometry used in the Dynamic Kinetic Monte Carlo simulation.

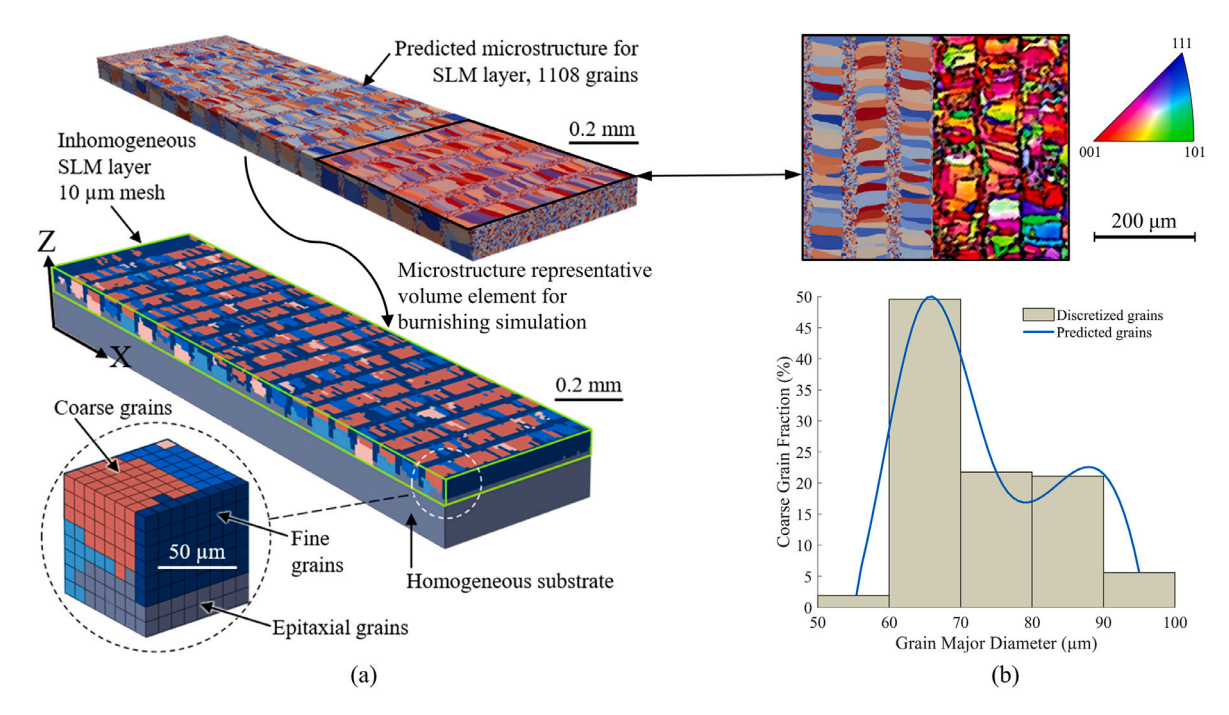


Fig. 5. (a) (*Top*) Inhomogeneous microstructure predicted by the Dynamic Kinetic Monte Carlo simulation within the domain of the subset identified in the laser powder bed fusion model (Ref. Fig. 2). The microstructure is depicted using different colors for individual grains to facilitate visualization, and color repetitions correspond to common spin numbers for lattice sites. (*Bottom*) Discretized microstructure representative volume element to be used for the interlayer burnishing simulation. (b) (*Top*) Comparison of the predicted microstructure with EBSD imaging from [63]. (*Bottom*) A comparison of the predicted and discretized coarse grain fractions based on grain major diameter. (For interpretation of the reference to color in this figure, the reader is referred to the online version of this article).

for individual grains to facilitate visualization, and color repetitions correspond to common spin numbers for lattice sites. Each grain's major and minor diameters are computed by a spherical fit algorithm. The simulated microstructure featuring alternating bands of coarse and refined grains obtained via DKMC is similar to that experimentally observed by [63,64], wherein grain sizes varied from 10 to 100 μm. Reconstructing each grain in an FE model of the subset for subsequent simulations, as seen in Fig. 5a (Bottom), is achieved via Python scripting. Material definitions based on grain-boundary strengthening considering each grain's major diameter can be applied to volumes of elements in the FE model representing the individual reconstructed grains, thereby generating a representative volume element. It should be noted, however, that this practice leads to a tremendous (if not impractical) increase in computational expense. With a marginal loss in accuracy, the predicted grains can be grouped (or discretized) into bins based on their major diameters as seen in Fig. 5b (Bottom). In the demonstrated work, a bin width of 10 µm is chosen to discretize predicted (coarse) grains with major diameters between 50 to 100 µm, thereby creating 5 bins (or groups) of grains, each having a unique material definition, MAT_i, based on the mean major diameter, d_i , in the ith bin. Bands of finer, relatively equiaxed grains (dark blue color) that form along the scan lines, having diameters ranging between 10 to $20 \mu m$, are grouped into a separate bin (not included in Fig. 5b) with its own material definition. Additionally, smaller spherically shaped grains predicted to be sporadically distributed at the base of the fused layer, with diameters also ranging between 10 to 20 µm, are considered to represent regions of the substrate that exhibit re-melting with epitaxial growth and hence are given the same material definition as the homogeneous substrate. In summary, 1108 grains with their individual material definitions are reduced to 7 groups. The loss in accuracy varies according to choice of bin width. The FE model for the subset, discussed in more detail later in Section 3.2, employs a 10 µm mesh to discretize the fused layer, hence, using bin widths any smaller in size would be redundant. Note, a few elements need to span the minor diameter of each reconstructed grain in the representative volume element to avoid a crash in any subsequent simulation due to zero-volume errors.

Using a smaller element size greatly increases computational cost, and grouping grains into bins prior to modeling the representative volume element, rather than reconstructing them individually, helps mitigate the occurrence of such errors.

A recent experimental investigation by Serrano-Munoz et al. (2021) [65] illuminated the effects of the emerging inhomogeneous microstructure on PBF-LB residual stress and inhomogeneous/anisotropic material response. Although, as described in Section 3, the inhomogeneous/anisotropic material response is captured during the burnishing simulation in accordance with the primary goals of the work herein, the PBF-LB modeling framework does not include inhomogeneity/anisotropy during prediction of the residual stress inherent to the PBF-LB process; hence, insights from Serrano-Munoz et al.'s work motivate further development of the numerical modeling capabilities for future studies.

3. Interlayer burnishing model

Once the laser scans for a given layer are performed, a roller-burnishing pass is executed to complete the hybrid cycle, prior to the subsequent powder layer deposition. The interlayer burnishing process features a 2.5 mm diameter tungsten carbide roller that performs a single pass over the newly melted layer. As illustrated in Fig. 6, the roller-workpiece penetration depth is assigned as 7 μm based on the average roughness measurements taken from the top surface of SLM Inconel 625 specimens subjected to multiple power and scan speed settings, documented by [66,67]. The coefficient of friction, μ , between the roller and the fused top surface, is assigned as 0.31 [68]. The roller velocity, $v_{\rm F}$, is assigned as 42.4 mm s $^{-1}$, with an angular velocity, $\omega_{\rm y}$, of approximately 33.93 rad s $^{-1}$, and a net vertical load ${\rm F}_z$ of 2 kgf (or 19.62 N) is distributed uniformly across the length of the roller. Table 4 summarizes the parameters used in the demonstrated interlayer burnishing simulation.

When a new layer is deposited and subsequently melted, remelting of previously fused layers might occur. In such cases, nucleation and

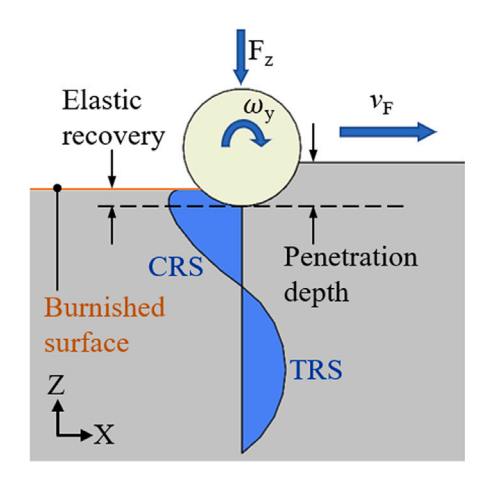


Fig. 6. Schematic of the interlayer burnishing simulation.

Table 4Summary of interlayer burnishing parameters.

| | 0 1 |
|---------------------------------------|----------------------------|
| Parameters | Values |
| Roller diameter | 2.5 mm |
| Penetration depth | 7 μm |
| Coefficient of friction, μ | 0.31 |
| Roller feed, $v_{\rm F}$ | 42.4 mm s^{-1} |
| Roller angular velocity, ω_{v} | 33.93 rad s^{-1} |
| Vertical load, F _z | 1 kgf (×2) |

recrystallization in the lower layers would accompany the process. Unsurprisingly, the near-surface compressive residual stress (CRS) induced during the previous burnishing cycle could vanish, yet as is shown later in Fig. 15, the burnishing induced CRS can penetrate well below $200 \mu m$ into the depth, hence its effect would not be entirely lost. Thus, interlayer/intermediate layer burnishing (or other treatments) may address the TRS build up that is known to occur in PBF-LB processes. Burnishing applied only as a post-process, however, does not address such accumulated build-up of TRS. Research into reduction in the accumulated distortion via interlayer/intermediate layer treatments is also actively being pursued for similar reasons [69]. Additional potential benefits of the intermediate treatment may include pore closure and more uniform thickness of the subsequently deposited powder layers. Accordingly, numerous research efforts involving a variety of means to induce plastic deformation (e.g., burnishing, laser shock peening) are being undertaken to investigate custom interlayer/intermediate layer treatments.

3.1. Residual stress mapping using natural neighbor interpolation

As discussed earlier, to reduce the computational expense, RS is only examined over a subset of the scanned volume, during the interlayer burnishing process. Hence, the burnishing model will need to map any pre-existing (or inherent) RS, arising from the PBF-LB simulation, as an initial state. This mapping is achieved via *natural neighbor interpolation*. The spatial interpolation method, introduced by Sibson (1981) [70], is based on Voronoi tessellation of discrete datapoints in Euclidean space. Unlike distance based spatial interpolation methods, the weighting factors are calculated based on Delauney triangulation of the nearest M "known" datapoints, spatially located such that they form a convex hull around the "point of interest" [71]. As given in Eq. (14), G(X) is data interpolated (or mapped) at location X (point of interest), where $\mathbf{w}_i(\mathbf{X})$ are *Laplace weights* [72] calculated by Eq. (15) with respect to location X, and $f(\mathbf{X}_i)$ is known data at convex hull location \mathbf{X}_i .

$$G(\mathbf{X}) = \sum_{i=1}^{M} w_i(\mathbf{X}) f(\mathbf{X}_i)$$
(14)

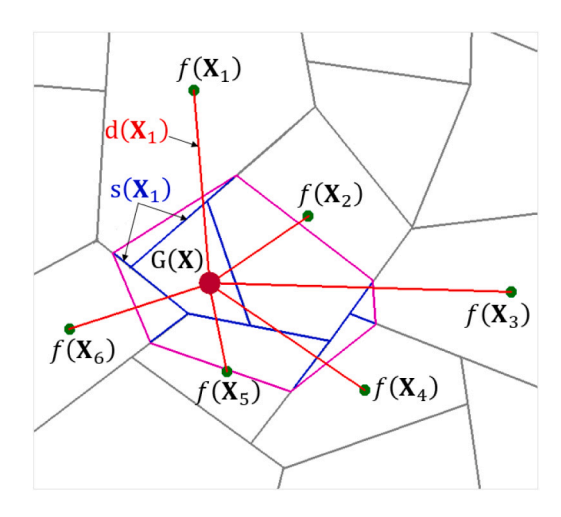


Fig. 7. Natural neighbor interpolation. Note, $s(\mathbf{X}_i)$ are treated as interface boundary lengths in 2D and surfaces in 3D.

In Eq. (15), $s(X_i)$ measures the 3D surface interface between the cells linking X and X_i , while $d(X_i)$ is the shortest distance between X and X_i , as depicted in Fig. 7.

$$w_{i}(\mathbf{X}) = \frac{\frac{s(\mathbf{X}_{i})}{d(\mathbf{X}_{i})}}{\sum_{j=1}^{M} \frac{s(\mathbf{X}_{j})}{d(\mathbf{X}_{j})}}$$
(15)

As discusses earlier, when reconstructing the microstructure representative volume element in the FE model, each grain requires a few elements to span its minor diameter to avoid zero-volume errors during plastic deformation in the burnishing simulation. Having very small elements in the PBF-LB simulation increases the number of solutions to be calculated at every time increment, thereby increasing computational expense. Mapping helps avoid this problem; while a coarser 25 μm mesh is used to model the powder layer being fused in the PBF-LB simulation, solutions of the AM process, including RS, distortion, and temperature fields, can be mapped to a finer 10 μm mesh for the interlayer burnishing simulations that follow. Note, in the demonstrated work only RS from the PBF-LB process is mapped as the initial state of the subset used in the thermomechanical interlayer burnishing model, discussed next.

3.2. Thermomechanical modeling of the interlayer burnishing process

Thermomechanical modeling of the interlayer burnishing process can be represented by Eqs. (1)–(10) with the exception of Eq. (2). As seen in Fig. 5a, a 10 μm mesh is used to model the 50 μm thick SLM layer. This is followed by another 30 μm thick layer wherein re-melting of the substrate's surface is assumed with epitaxial grain growth as mentioned earlier. Beneath this are two layers of 60 μm long elements to model the Inconel 625 substrate which is assumed to have a relatively homogeneous microstructure. The AM part and the deformable roller modeled for the burnishing process feature linear hexahedral coupled temperature displacement elements.

The inherent RS in the AM part at the end of the scans for a given layer is mapped as the initial state for the burnishing pass that follows, as given by Eq. (16), where σ_{AM} and σ_{IB} represent, respectively, the stress fields from AM of one layer, and the subsequent interlayer burnishing processes during a single hybrid cycle.

$$\sigma_{\rm IB}(\mathbf{X}, 0) = \sigma_{\rm AM}(\mathbf{X}, t_{\rm end}) \tag{16}$$

Taking Eq. (14) into consideration, Eq. (16) can be expressed as Eq. (17).

$$\sigma_{\rm IB}(\mathbf{X},0) = \sum_{i=1}^{M} w_i(\mathbf{X}) \sigma_{\rm AM}(\mathbf{X}_i, t_{\rm end})$$
(17)

To assess the influence of temperature on magnitude of RS induced during burnishing, the burnishing process is performed at temperature, $T_{\rm IB}$, per Eq. (18). The effects of warm interlayer burnishing temperatures, $T_{\rm IB}$ (296 K, 573 K, and 873 K), are parametrically examined in this work, as detailed later in Section 4.

$$T(\mathbf{X},t) = T_{\rm IB}, \quad \text{for} \quad t \ge 0 \tag{18}$$

During the burnishing process, friction between the fused layer and the roller can generate small amounts of heat. Equation 19 describes the heat, q_{Cf} , generated due to Coulomb friction as a function of the plastic heat dissipation fraction, η (assumed to be 0.9), coefficient of friction, μ , slip rate \dot{s} [73], and the tool-workpiece interface contact pressure, p.

$$q_{Cf} = \eta \mu p \dot{s} \tag{19}$$

In addition, a fraction of the total heat generated, q_p , described by Eq. (20), stems from the mechanical heat dissipation due to plastic strain, σ : $\dot{\epsilon}_p$, as the burnishing roller passes over the material.

$$q_{p} = \eta \sigma : \dot{\varepsilon}_{p} \tag{20}$$

Considering the motion of the burnishing roller, displacement boundary conditions are imposed on multiple surfaces of the subset as described by Eq. (21).

$$\begin{array}{ll} U_X=0, & \text{on surfaces } X=0 \text{ and } 2 \text{ mm} \\ U_Y=0, & \text{on surfaces } Y=0 \text{ and } 0.5 \text{ mm} \\ U_Z=0, & \text{on surface } Z=0 \end{array} \tag{21}$$

3.3. Material modeling for interlayer roller-burnishing simulation

The thermomechanical material properties used for (solid) Inconel 625 during the PBF-LB process remain unchanged during the interlayer roller-burnishing simulation. Anisotropy that arises from the inhomogeneous microstructure is defined by introducing a temperature and strain-rate sensitive Johnson–Cook plasticity model [74], wherein the flow stress, $\sigma_{\rm f}$, for grains having different major diameters, varies based on Hall–Petch strengthening [75–78]. Equations 22–24 describe the material modeling approach.

$$\sigma_{\rm f} = \left[A + B \varepsilon_{\rm p}^{n} \right] \left[1 + C \ln \left(\frac{\dot{\varepsilon}_{\rm p}}{\dot{\varepsilon}_{\rm 0}} \right) \right] \left[1 - \left(T^{*} \right)^{m} \right] \tag{22}$$

$$T^* = \begin{cases} 0, & T < T_0 \\ \left(\frac{T - T_0}{T_m - T_0}\right), & T_0 \le T \le T_m \\ 1, & T > T_m \end{cases}$$
 (23)

$$\mathbf{A} \equiv \sigma_{\mathrm{y,i}} = \sigma_0 + \frac{k_y}{\sqrt{d_\mathrm{i}}} \tag{24}$$

In Eqs. (22) and (24), A is the yield strength empirically determined via the Hall–Petch relation, in which any stress exceeding σ_0 can initiate dislocation movement, with k_y being the strengthening coefficient, and d_i being the mean major diameter for the i^{th} bin of grains obtained as described in Section 2.4. As mentioned earlier, grouping the grains into bins and considering an average diameter to represent the grains in the respective bin, rather than computing Eqs. (22)–(24) based on individual grains' major diameters, introduces a marginal loss of accuracy. In the demonstrated work the average error introduced in the calculation of yield strength is ~1.46%. Material parameters for the combined Johnson–Cook Hall–Petch approach are listed in Table 5, [79–81]. Note that the density and Young's modulus for Inconel 625 shown in Table 5 are only for room temperature. Temperature dependent properties as per [6,46] have been used in the burnishing simulation.

Table 5
Material properties for the Inconel 625 subset and the tungsten carbide burnishing roller, [79–81,84,85].

| Material Properties | Inconel 625 subset | Tungsten carbide burnishing roller |
|-------------------------------|--------------------------------|------------------------------------|
| Density (kg m ⁻³) | 8440 | 13560 |
| Young's modulus (GPa) | 208 | 480 |
| Poisson's ratio | 0.3 | 0.22 |
| Hall-Petch parameters | | |
| σ_0 (MPa) | 105 | _ |
| k_{v} (MPa $\mu m^{0.5}$) | 1380 | _ |
| Johnson-Cook plasticity p | oarameters | |
| A (GPa) | $\sigma_{\rm v.i.}$ (Eq. (24)) | 3.6 |
| B (GPa) | 2.2013 | 5.49 |
| C | 0.000209 | 0.09 |
| $\dot{\varepsilon}_0(s^{-1})$ | 1670 | 1 |
| n | 0.8 | 0.4 |
| m | 1.146 | 1.74 |
| T _m (K) | 1898 | 3143 |
| T ₀ (K) | 296 | 296 |

A tungsten carbide roller is considered for the roller-burnishing application [82] given its high strength and hardness, low coefficient of friction at high melting temperature which promotes better wear resistance under high friction and temperature conditions [83]. A Johnson–Cook plasticity model is also used for the roller. Material properties for the roller are listed in Table 5, [84,85].

A summary of the demonstrated modeling approach for interlayer burnishing, featuring mapping of inherent RS, as well as reconstruction of the inhomogeneous microstructure arising from the PBF-LB process, is presented in Fig. 8. Results of the burnishing simulation, examining the influence of microstructure modeling, inherent RS and environment temperature, on the induced RS along the surface and through the depth of the subset are discussed next.

4. Results and discussion

4.1. Laser powder bed fusion inherent stress

During the laser scanning process, the state of stress fluctuates between compressive and tensile while the MP and HAZ are in close proximity to any point in the fused layer. In comparison to the magnitudes of longitudinal stress, $\sigma_{\rm V}$, and transverse stress, $\sigma_{\rm X}$, the stress in the depth direction, σ_Z , is relatively lower in magnitude given that only one layer is simulated in this work. Hence, the results discussed herein focus on the longitudinal and transverse components along the surface as well as at various depths beneath the scanned surface. Figure 9(a) depicts the history of σ_Y and σ_X for Node 1 (Ref. Fig. 4(a)) during the laser scan process prior to burnishing. Fluctuating tensile and compressive peaks seen in the stress history of Node 1 occur concurrently with the peaks in the thermal history. The overall trend in stress history is similar for all the nodes in the scanned region of the FE model in that extreme fluctuations (or oscillations) between compressive and tensile magnitudes transpire while the MP and HAZ are in close proximity, however, these oscillations decay to reveal a highly tensile state of stress in the fused layer. Referring to Fig. 9(a), a considerable difference exists in the peak tensile and compressive stress magnitudes, for both $\sigma_{\rm Y}$ and $\sigma_{\rm X}$, during the oscillatory phase; $\sigma_{\rm Y}$ ranges from approximately -0.9 GPa to 0.77 GPa, whereas, $\sigma_{\rm X}$ ranges from approximately -0.57GPa to 0.39 GPa. Once the oscillations decay, the tensile state of stress that emerges for both components, also reveals significant difference; $\sigma_{\rm Y}$ is approximately 0.73 GPa, whereas, $\sigma_{\rm X}$ is approximately 0.31 GPa. Trends in the predicted RS closely match those numerically determined and experimentally validated by Denlinger et al. [44], whose PBF-LB studies similarly featured a bi-directional scanning pattern. The tension is attributed to rapid cooling and contraction of the material, once it has been scanned and melted (or fused) by the laser. The TRS induced in the

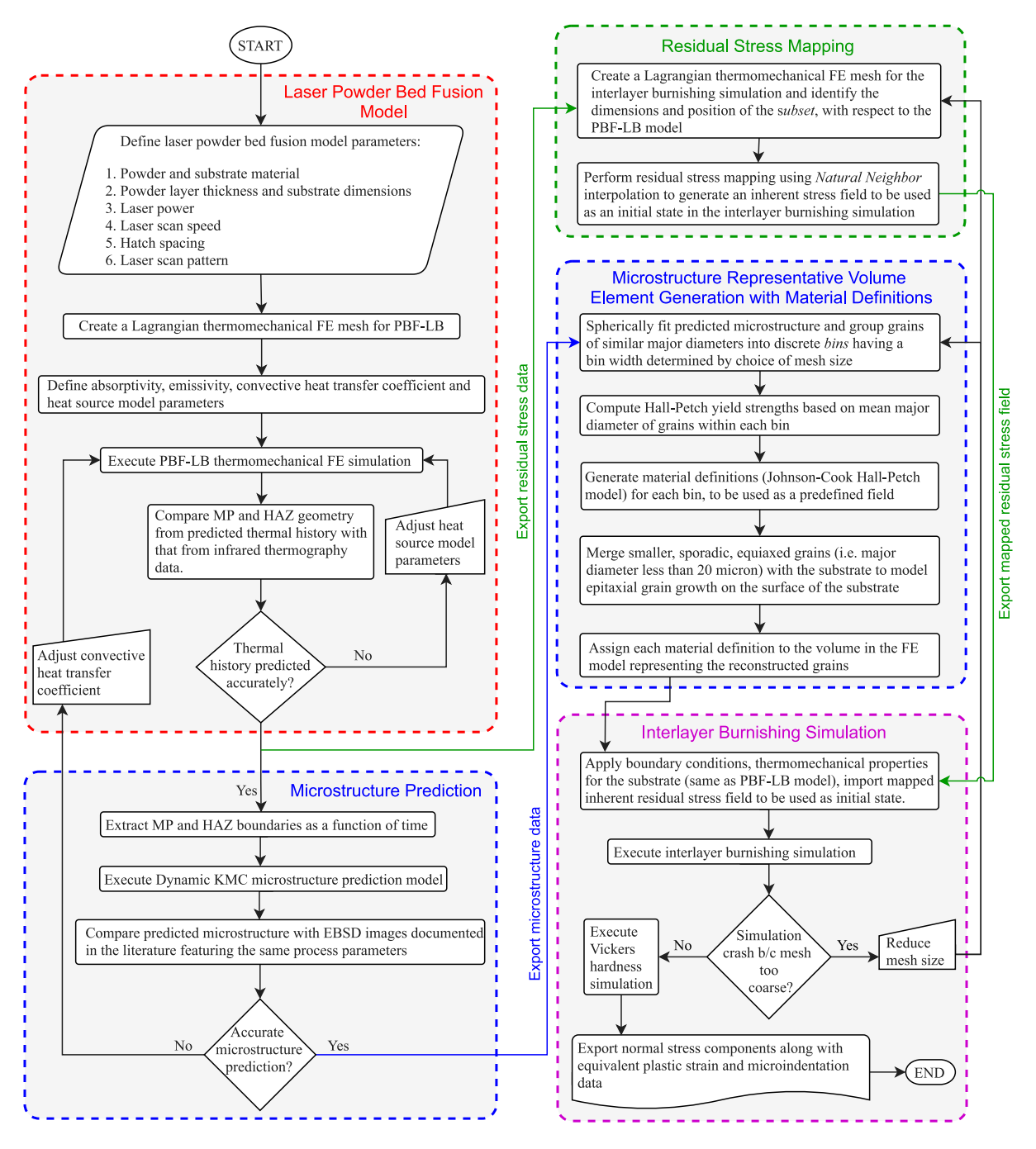


Fig. 8. Flowchart summarizing the modeling framework for the described hybrid additive manufacturing process that combines selective laser melting with roller burnishing, capturing the effects inherent residual stress and inhomogeneous microstructure.

fused layer forces regions deeper within the substrate toward a state of compression to balance the RS distribution [7]. In the present work, as well as in that of Denlinger et al. TRS in the longitudinal direction (Y) is significantly greater than that predicted in the transverse direction (X), analogous to findings documented in welding literature [86,87].

As noted earlier, to reduce computational expense, a smaller subset region of the PBF-LB FE model is used for the interlayer burnishing simulation. Inherent residual stresses and microstructure are mapped from the PBF-LB model to the mesh of the subset for the subsequent burnishing FE model. Figure 9(b) illustrates the inherent longitudinal stress component, $\sigma_{\rm Y}$, from PBF-LB which is mapped as an initial state for burnishing. As depicted earlier in Fig. 6, the burnishing roller's axis is parallel to the Y-axis, and the roller traverses the surface of the subset along the X-direction, hence for the subsequent interlayer burnishing

simulation, σ_Y represents the axial component of burnishing induced RS, while σ_X represents the component in the rolling direction (X). In this work, the rolling and axial components of burnishing induced RS are studied along a 2 mm path across the length (X) of the subset, as well as through the thickness (Z) of the subset, analogous to XRD measurements, wherein the each RS component is averaged over a 0.3 mm \times 0.3 mm region, for multiple depths from the surface, as seen in Fig. 9(b).

Figure 9(c) shows the variation in magnitudes of σ_Y and σ_X along the path on the surface of the subset prior to interlayer burnishing. Along the surface, the tensile residual stress range in the longitudinal direction ($\sigma_Y = 0.8$ to 1 GPa) is found to be significantly greater than that seen in the transverse direction ($\sigma_X = 0.2$ to 0.44 GPa). In addition, σ_Y reveals a periodicity, that is not present in σ_X . The peaks of adjacent

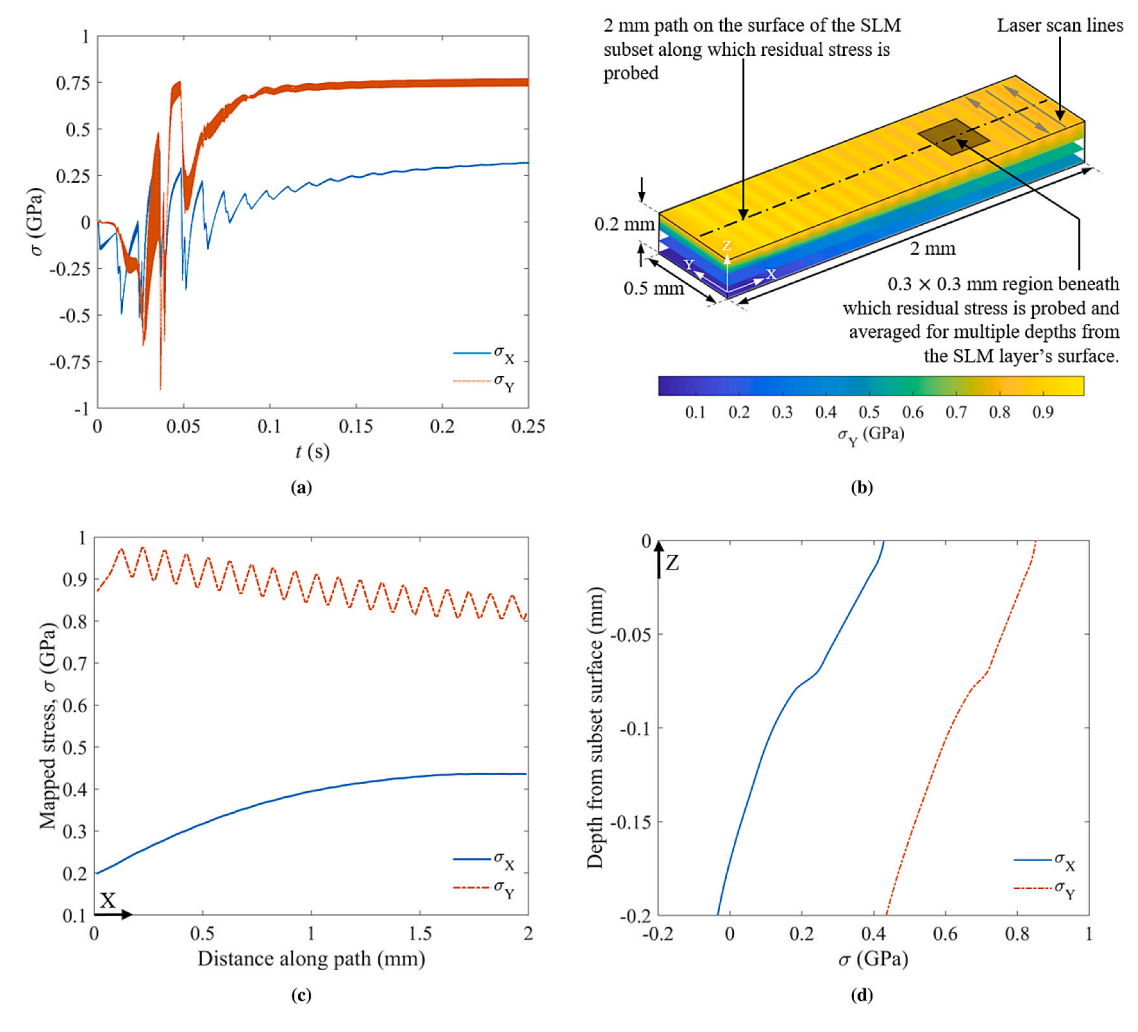


Fig. 9. (a) Transverse (σ_X) and longitudinal (σ_Y) stress history for Node 1 (14.15, 11, 3.2 mm) during the PBF-LB simulation (Ref. Fig. 2). (b) Illustration depicting 3D longitudinal stress distribution in the subset. A 2 mm path is shown across the length of the surface along which surface stresses will be examined in this work. A 0.3 × 0.3 mm patch is also depicted within which predicted stress components are averaged similar to XRD measurements, for multiple depths. (c) Stress components along the 2 mm path on surface of the subset after the laser scans. (d) Components of stress averaged over the 0.3 × 0.3 mm patch through the depth of the specimen.

crests in $\sigma_{\rm Y}$ lie on points that are located directly upon laser scan lines, i.e., wavelength 100 µm apart with an average wave height of 72 MPa. This wave height would increase with a larger hatch spacing. The TRS arises because the heat source head, moving with a particular velocity (800 mm s⁻¹, ±Y direction), causes material expansion in its vicinity (in almost the same direction that the head is moving), while at the other end of the scan line, rapid cooling and contraction pulls material in the opposite direction. The same phenomenon occurs for $\sigma_{\rm X}$, however, its tensile magnitude is comparatively lower given that the scan progression (Ref. Fig. 2) in the transverse direction occurs at a considerably slower rate (16 mm s⁻¹, -X direction).

Figure 9(d) shows the area-averaged magnitudes of σ_Y and σ_X through the thickness (Z) of the subset prior to interlayer burnishing. Clearly, the tensile character observed along the surface reduces with depth in order to balance the RS distribution. It is also observed that the magnitude of σ_Y is significantly greater than that of σ_X throughout the depth. Note that the original FE model used in the PBF-LB simulation is 3.2 mm thick and only the upper 0.2 mm is used for the subset, as seen in Fig. 9(b). In the PBF-LB simulation both, σ_Y and σ_X , become compressive in character deeper within the substrate.

4.2. Parametric studies for interlayer burnishing

The demonstrated interlayer burnishing simulation seeks to elucidate the influences that microstructure modeling, mapping of PBF-LB

inherent RS (as an initial state), and environment temperature have on the state of stress induced via the interlayer burnishing process. To achieve this, six different cases, that comprise two parametric studies, are simulated as listed in Table 6. The first parametric study, involving Cases 1 to 4, examines the respective influences of microstructure and PBF-LB inherent RS, while the second parametric study, involving Cases 4 and 5, examines the effects of warm interlayer burnishing temperatures, T_{IR}, on the state of burnishing-induced RS. Three warm burnishing temperatures, 296 K (23 °C), 573 K (300 °C) and 873 K (600 °C), are studied in the demonstrated work bearing in mind the influence of temperature on toughness. Inferences made from experimentally obtained stress-strain response of Inconel 625 at elevated temperatures documented by Oliveira et al. [88] and Ziaja et al. [89] reveal that the modulus of toughness reduces when the material is subjected to higher temperatures. Considering Ziaja et al.'s stress-strain response (0.0005 s⁻¹), the calculated toughness between 296 K to 900 K is 350 MJ m⁻³ after which it almost linearly reduces to 116 MJ m⁻³ (at 1173 K). While the yield strength of the alloy reduces significantly for temperatures exceeding 900 K, meaning less vertical load, F_z, would be required to induce the same amount of plastic deformation on the fused surface, this undesirably increases the likelihood of micro-crack formation and occurrence of fractures during the interlayer burnishing pass, thereby having a detrimental effect on the overall macroscopic strength (and perhaps performance) of the AM part.

Table 6Summary of burnishing case studies investigated.

| - | · · | U | |
|------|----------------|-----------------|-----------------------|
| Case | Microstructure | PBF-LB Residual | Interlayer Burnishing |
| | Modeling | Stress Mapping | Temperature, T(K) |
| 1 | | | 296 |
| 2 | | | 296 |
| 3 | | | 296 |
| 4 | | | 296 |
| 5 | | | 573 |
| 6 | | | 873 |

Furthermore, during hot deformation, i.e., T > 1223 K (or 950 °C). dynamic recrystallization (DRX) can occur in Inconel 625 [90]. Elevated temperatures, as well as lower strain rates are found to promote (and accelerate) the DRX process, while the thermal softening causes the alloy's flow stress to reduce significantly [91]. Given the face center cubic crystal structure of Inconel 625 and a calculated stacking fault energy of approximately 215 mJ m⁻² [92], dislocation slip and twinning are the most common modes of deformation. Dislocation slip occurs primarily during the initial stages of deformation, followed by twinning during the later stages. At elevated temperatures, an increased grain boundary mobility is found to result in the nucleation of twins. The twin boundaries formed between recrystallized grains can progressively transform into high angle grain boundaries, thus promoting the nucleation mechanism for DRX [26,93]. A limitation of the presented framework is that DRX is not modeled, nor is a subroutine implemented to update the Johnson-Cook flow stress parameters during the burnishing simulation, as this would greatly increase the computational cost. Hence, DRX phenomena is not captured in the demonstrated framework. This should not present any errors as the highest simulated temperature is 873 K considering the effect of temperature on toughness.

4.3. Yield criterion and equivalent plastic strain on the burnished surface

Incorporating the inhomogeneous PBF-LB microstructure representative volume element in the burnishing FE model enables the prediction of stress concentrations and equivalent plastic strains that arise among the fine grains that fall along the scan lines. As discussed earlier, the inhomogeneous microstructure is implemented by means of a unique yield strength calculated for each bin of grains, having a unique (averaged) major diameter, per Hall-Petch strengthening [75,76]. In effect, a unique maximum distortion-energy criterion will exist for each bin of grains. This can be visualized as a unique elliptical yield surface for each bin. A collection of all the individual yield surfaces for the coarse grain bins and/or fine grain bins appear as a band as depicted in Fig. 10. Figure 10 illustrates a band of maximum distortion-energy yield surfaces (blue) for the fine equiaxed grains found along the scan lines and the homogeneous substrate, with diameters of approximately 10 to 20 μm, as well as another band of yield surfaces (red) representing the coarse grains that emerge in the inhomogeneous fused layer, between successive scan lines, with diameters ranging from 50 to 100 µm.

To help understand the influence of modeling the fused layer with an inhomogeneous microstructure having varying yield surfaces, equivalent plastic strain, $\gamma_{\rm eq}$, is predicted and examined along the 2 mm path on the burnished surface of the subset, as seen in Fig. 11. A monotonic increase in $\gamma_{\rm eq}$ is said to occur whenever the localized state of stress in the alloy is on the yield surface. Figure 11 depicts a parametric study on the influence of microstructure and inherent residual stress on $\gamma_{\rm eq}$ across the burnished surface. Cases 2 and 4 include microstructure effects and appear considerably different in comparison to Cases 1 and 3, which do not include microstructure. A non-uniform $\gamma_{\rm eq}$ distribution is evident in Cases 2 and 4, as seen in Fig. 11; while almost identical to one another, Cases 2 and 4 exhibit a periodicity along the X direction with a wavelength of ~100 μ m associated to the PBF-LB scan lines.

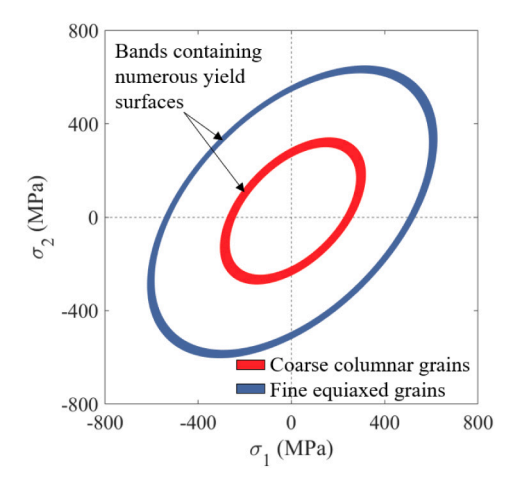


Fig. 10. Bands representing the ranges of numerous maximum distortion-energy yield surfaces for the coarse columnar and fine equiaxed grains. Each unique yield surface encompassed within these bands is used in the material definition to represent a specific grain major diameter within the representative volume element subset of the interlayer burnishing simulation.

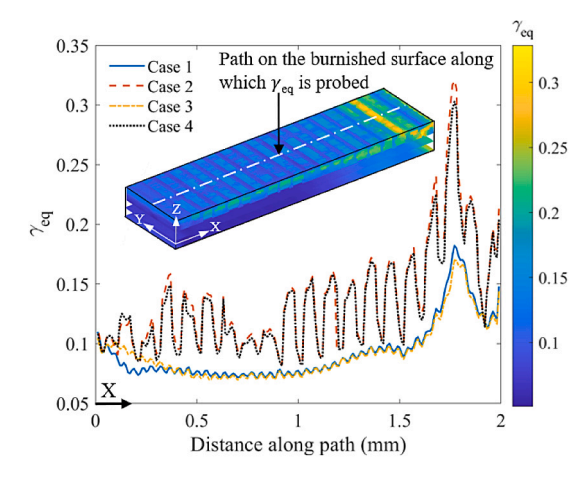


Fig. 11. Equivalent plastic strain, γ_{eq} , along the 2 mm path across the subset's surface. Note, the inset 3D contour plot corresponds to Case 4 (Ref. Table 6).

The overall magnitude of γ_{eq} for Cases 2 and 4 is clearly greater in comparison to that for Cases 1 and 3. A small but distinct oscillation is seen in Cases 1 and 3. This should not be mistaken as a phenomena that arises from the PBF-LB process. It is an inaccuracy that stems from burnishing FE model when using a relatively coarser mesh to discretize the circumference of the roller in comparison to that used to discretize the length of the subset. Using a relatively finer mesh for the roller can help mitigate this problem, however, it would effectively increase the computational expense. Note that a similar spurious oscillation also affects the predictions for Cases 2 and 4, but given the magnitude of γ_{eq} , its presence is not as evident.

When comparing Cases 3 and 4 with Cases 1 and 2, respectively, the incorporation of a mapped inherent RS field from PBF-LB as an initial state to burnishing appears to have a relatively smaller influence on the $\gamma_{\rm eq}$ predictions in comparison to the effects from including microstructure. The large peak seen at a distance of $\sim\!1.75$ mm along the path corresponds to material being compressed between the roller and the fixed boundary on plane X = 2 mm, preventing the subset from sliding in the +X direction during burnishing.

4.4. Residual stress induced along the burnished surface

The periodicity and spurious oscillations predicted for $\gamma_{\rm eq}$ also extend to the state of RS on the burnished surface in the rolling direction, σ_X , and the axial direction, σ_Y , as seen in Figs. 12(a) and 12(b), respectively. The line plots depict stress along the 2 mm path on the burnished surface of the subset for the parametric study investigating the influence of microstructure modeling and inherent RS mapping. For both, σ_X and σ_Y , Cases 2 and 4 (which consider microstructure modeling) reveal a periodicity along the X direction with a wavelength of $\sim 100~\mu m$ (equivalent to the PBF-LB hatch spacing). The troughs in these waves align with the darker bands in the inset contour plots of the subset's burnished surface, clearly indicating intermittent regions of high compressive peaks along the length. These regions fall along the PBF-LB scan lines and hence consist of finer, equiaxed grains. Compared to the columnar grains found in the hatch (Ref. Fig. 5a), the equiaxed grains have a smaller averaged diameter and hence a greater yield stress, per Hall-Petch strengthening [78]. This results in a relatively higher flow stress along the scan line in comparison to regions within the hatch space. Consequently, the CRS induced along the surface via plastic deformation during the interlayer burnishing pass exhibits a pattern of alternating compressive peaks. Note that the inset contour plots presented in Fig. 12 correspond to Case 4.

While Cases 2 and 4 are very similar, a subtle difference arises due to the mapped inherent RS field implemented in Case 4. Cases 1 and 3 (which neglect microstructure modeling) are also almost identical, with a subtle difference associated to the inherent stress mapping performed in Case 3. They do not share the same banded contour pattern on their respective burnished surface. While similar to Cases 2 and 4 in overall RS magnitude, Cases 1 and 3 only reveal the spurious oscillations discussed earlier. These oscillations also manifest in Cases 2 and 4, however, the effect is far less evident if not entirely masked considering the amount of variation in RS (or wave height) attributed to microstructure inclusion in the modeling framework.

Analogous to Colegrove et al.'s findings [12], the TRS from PBF-LB seen in Fig. 9(c) is transformed to CRS, as seen in Fig. 12, during the burnishing pass. Excluding the peak in RS toward the end of the subset, X>1.5 mm, which is formed as material near the plane X=2 mm is pinched between the fixed boundary and the roller, a seemingly consistent range in CRS is observed for both components. The magnitude of CRS induced in the rolling direction, σ_X , is clearly more compressive in character in comparison to that in the axial direction, σ_Y , along the surface. Considering Case 4, σ_X varies in the range of -1 GPa to -0.8 GPa, whereas σ_Y varies in the range of -0.55 GPa to -0.4

GPa. Furthermore, in both plots the limits of the vertical axis ($\sigma_{\rm X}$ and $\sigma_{\rm Y}$) differs from that of the color-bar representing the RS contours on the burnished surface. This suggests that while the predicted periodic trend in burnishing induced RS may not vary (considering the contours), the magnitude of RS will vary along different paths across the length of the burnished surface, parallel to one depicted (white line). The predicted results confirm the hypothesis inferred from Courbon et al.'s work [11] regarding the influence of microstructure of deposited material on the (post-burnishing) RS distribution, in that implementing the inhomogeneous microstructure introduces anisotropy in the surface RS distribution.

When assessing the effect of environment temperature on the burnishing induced surface RS, as seen in Figs. 13(a) and 13(b), two important observations are made:

- 1. The overall magnitude of induced CRS reduces with an increase in temperature. The elevated temperatures reduce the flow stress of the material, thereby reducing the amount of CRS that can be induced for approximately the same amount of strain (Ref. Fig. 11) as the burnishing roller passes over the material. Note that in the demonstrated Cases a slight non-linearity in the relationship between flow stress and temperature arises from the thermal softening parameter (*m* = 1.146) [79]. A similar stress relaxation effect resulting from elevated temperatures was also documented by Breidenstein et al. [19], albeit for TRS during the SLM process.
- 2. The microstructure driven periodicity in RS associated to the SLM scan lines remains the same, however, the wave height indicative of RS in regions of finer equiaxed grains (along scan lines) and coarser columnar grains (within the hatch space between consecutive scan lines) reduces significantly for Case 6 (873 K) as temperature increases. As discussed earlier, with an increase in temperature, toughness of the material reduces significantly, and a damage model would have to be introduced for temperatures exceeding ~900 K. Changes in the microstructure from DRX and twinning, when the temperatures exceed ~1223 K mean that the material definitions would require iterative updates via a subroutine. Grain boundary sliding (GBS) may offer a reasonable explanation for the relatively smaller wave height predicted for Case 6 (873 K) in comparison to Cases 4 (296 K) and 5 (573 K). Liu et al. determined that at approximately $0.5T_{m}$ (~784 K) GBS among fine equiaxed grains can be observed [94]. Such grains will emerge along scan lines, as was seen earlier in Fig. 5a. These fine grains typically contain a mix of high angle grain boundaries as well as low angle grain boundaries.

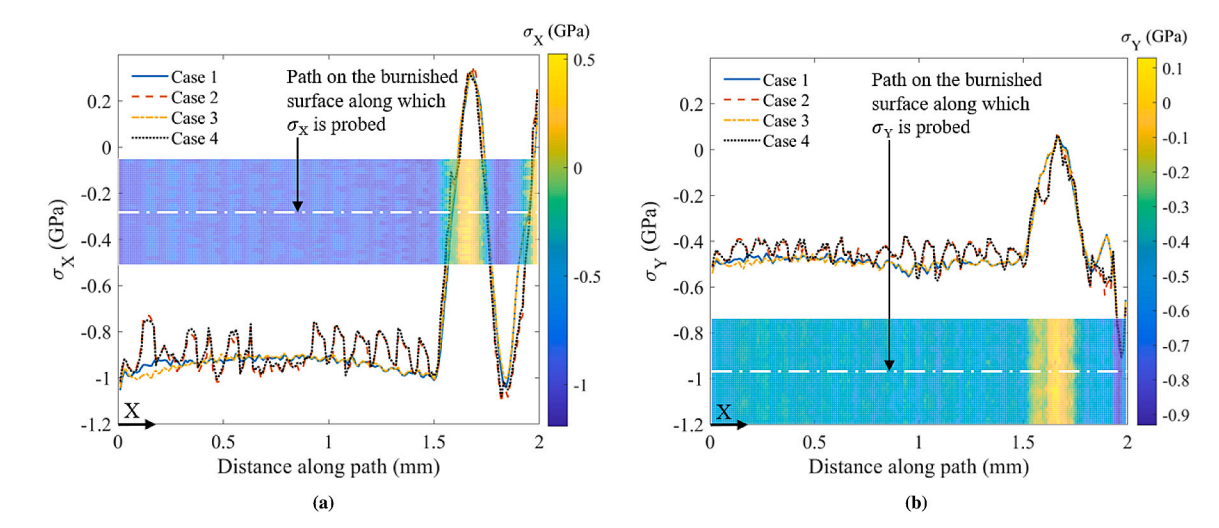
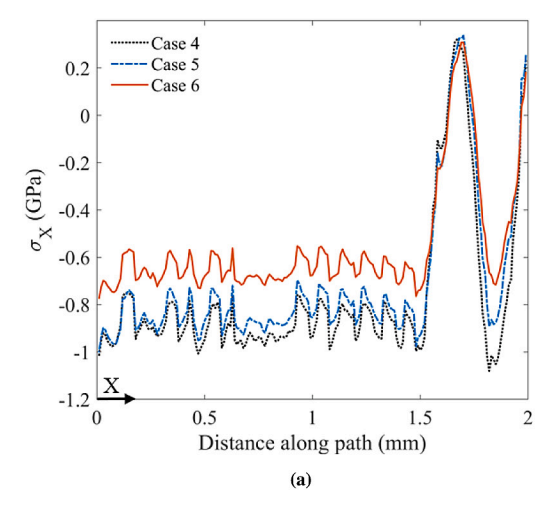


Fig. 12. Parametric study on the effect of microstructure modeling and inherent residual stress mapping on burnishing induced stress in (a) the rolling direction (X), and (b) the axial direction (Y), along the surface of the subset.



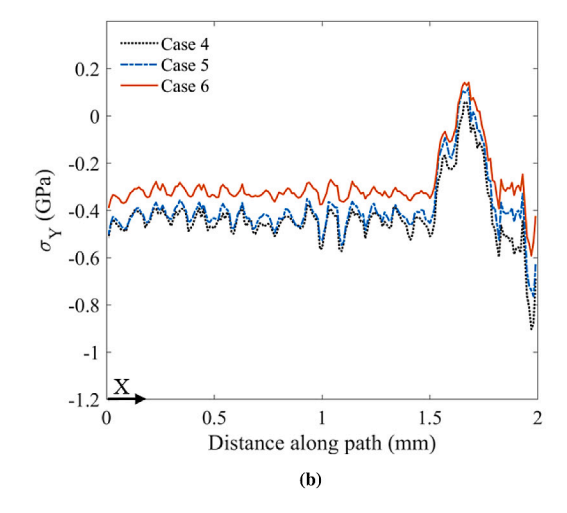


Fig. 13. Parametric study on the effect of temperature on burnishing induced stress in (a) the rolling direction (X), and (b) the axial direction (Y), along the surface of the subset. Case 4: 296 K, Case 5: 573 K, Case 6: 873 K (Ref. Table 6).

GBS readily occurs along high angle grain boundaries and is accompanied by random grain rotations when the material experiences extreme plastic deformation. During extreme plastic deformation finer grains may grow as well as change shape in order to prevent formation of cavities [95]. Larger grains located in the hatch spaces have lower yield strength per Hall-Petch strengthening, and will accordingly have a lower flow stress in comparison to the finer equiaxed gains that comprise the bands on the surface falling along SLM scan lines. These bands contain a higher density of grain boundaries (both high and low angle grain boundaries) in comparison to the hatch spaces. The higher density of grain boundaries promotes greater impedance to dislocation motion, thereby resulting in the induced CRS peaks during the burnishing pass. As temperatures exceed 0.5T_m, in addition to dislocation slip and DRX phenomena, GBS likely begins to occur among the finer grains (considering their relatively greater flow stress), thereby reducing the magnitude of the induced CRS peaks. Furthermore, when the alloy is subjected to strain rates exceeding its threshold strain rate for GBS, stress concentrations can develop at locations such as grain triple junctions, boundary ledges and even grain interiors, leading to intragranular plastic deformation as well as recrystallization when the material is in a state of CRS.

4.5. Residual stress induced through the depth

Figures 14(a) and 14(b), reveal the trends in averaged RS through the depth of the subset, whilst parametrically investigating the influence of microstructure modeling and inherent RS mapping. Comparing both rolling (σ_X) and axial (σ_Y) components, the compressive character of $\sigma_{\rm X}$ is observed to be significantly greater than that of $\sigma_{\rm Y}$. This is expected considering of the cylindrical contact surface, and orientation of the burnishing roller. Cases 2 and 4, which include inhomogeneous microstructure modeling for the first 80 µm from the surface, reveal very similar trends and magnitudes of CRS. The subtle difference observed between the two arises due to the inherent stress mapping. Case 3 appears to show a similar trend and magnitude of CRS to Cases 2 and 4 only after ~80 µm of depth from the surface, due to the fact that the substrate is considered to be homogeneous in all the Cases examined. For the first 80 µm from the surface, the magnitude of CRS predicted for Case 3 is found to be greater (more compressive) than that for Cases 2 and 4, by approximately 80 MPa. Furthermore, considerable differences exist in the predicted trends of Cases 1 and 3, illuminating the influence of inherent RS mapping. From the trend and magnitude

predicted for Case 4, it is evident that the microstructure modeling has a more significant influence in comparison to the RS mapping, albeit the effects of RS mapping are still observable and hence should not be neglected. When comparing trends for Case 4 between the rolling (σ_X) and axial (σ_Y) components of induced RS through the depth of the subset, σ_Y reveals a relatively sharper peak appearing closer to the surface, whereas σ_X shows a smoother peak appearing deeper beneath the burnished surface. These overall predicted trends resemble those from XRD measurements documented by Altan et al. who examined RS in roller-burnished AISI 52100, although the magnitudes of induced CRS differ considering differences in material and burnishing process parameters [1].

Figure 12 (surface RS) and Figs. 14(a) and 14(b) (through depth RS) parametrically illuminate the individual contributions of microstructure and inherent residual stress on the induced stress due to the burnishing process, and hence the figures elucidate the relative importance of each contribution. It is critical to note that experimental measurements of the individual contributions revealed in Fig. 12 (and Figs. 14(a) and 14(b)) are not possible to obtain since the microstructure and inherent residual stress contributions cannot be decoupled experimentally. Methods such as XRD reveal spatially averaged RS patterns, e.g., Figs. 14(c) and 14(d) [1], which do not offer any information on the decoupled (i.e., separate) contributions of the inherent RS and microstructure on the burnishing induced residual stress. In other words, the microstructure and inherent residual stress effects cannot be isolated experimentally to study their individual contributions. Even though heat treatment could be performed to alleviate the inherent stress, such treatment may alter the underlying microstructure and configuration of dislocations. Hence, the need for physics-based numerical investigation as presented here is evident. Nonetheless, as shown in Figs. 14(a)-14(d), the overall trends of the predicted postburnishing stress reveal good comparison to XRD measurement trends of other burnishing processes [1], even if the XRD cannot distinguish the individual effects previously described.

The magnitude of burnishing induced CRS significantly reduces with an increase in the environment temperature, as seen in Figs. 15(a) and 15(b). As mentioned earlier, this is expected due to a reduction in flow stress at elevated temperatures. The predicted trends seen in Fig. 15 are analogous to experimentally captured trends in stress relaxation via heat treatment documented by [96,97].

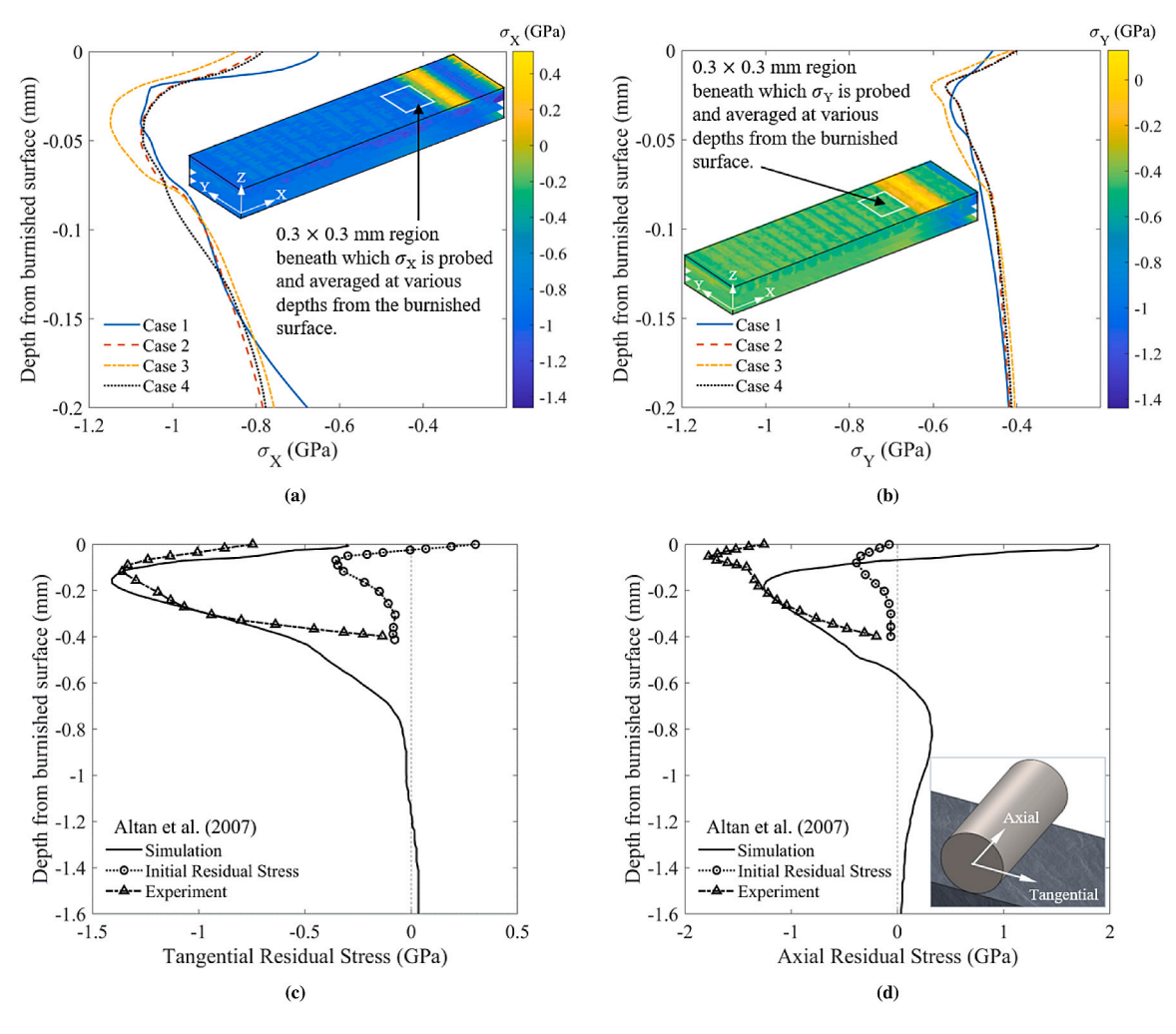


Fig. 14. Parametric study on the effect of microstructure modeling and inherent residual stress mapping on burnishing induced stress in (a) the rolling direction (X), and (b) the axial direction (Y), through the depth of the subset. Burnishing data adopted from a study by [1] for stress in (c) tangential (or rolling) direction, and (d) axial direction.

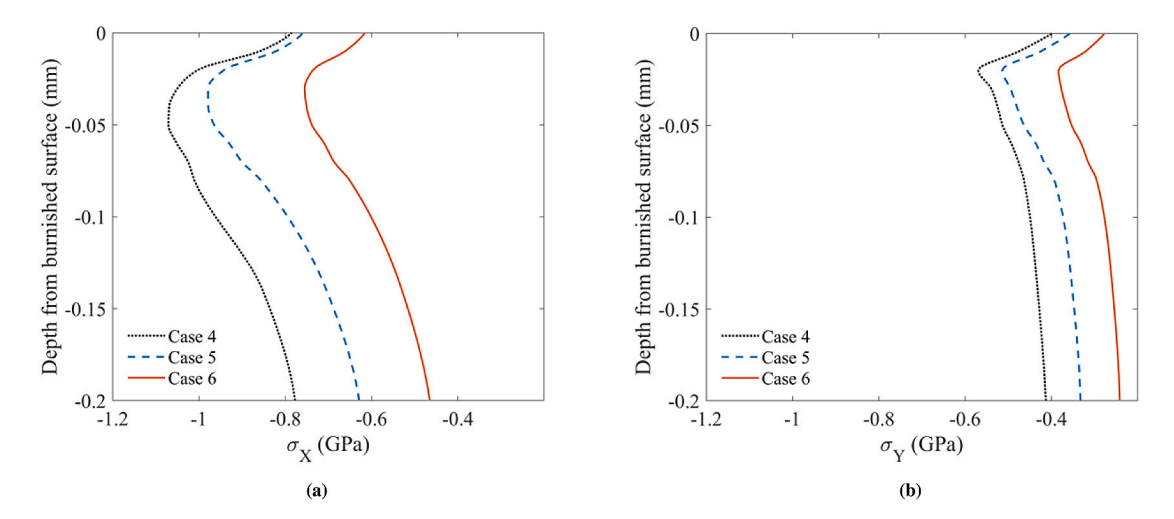


Fig. 15. Parametric study on the effect of temperature on burnishing induced stress in (a) the rolling direction (X), and (b) the axial direction (Y), through the depth of the subset. Case 4: 296 K, Case 5: 573 K, Case 6: 873 K.

The higher magnitudes of residual stress, exceeding the ultimate strength of IN625 as seen in Figs. 12-15, stem from the strain hardening behavior modeled in the material based on findings by Hokka

et al. [79]. Obtaining stress–strain curves for the material with higher ultimate strengths post-treatment is not uncommon for surfaces treated by rolling or burnishing processes [98].

4.6. Surface hardness

Microindentation simulations as per ASTM E384 [99,100] were also performed on Cases 4 to 6 (Ref. Table 6) to examine the influence of burnishing temperature on surface hardness. A Vickers indenter, with a load of 1 kgf (~9.81 N) was allowed to penetrate the surface of the burnished subset for up to 10 s, after which the average diagonal length from the indentation was used to compute the Vickers hardness number. Hardness predicted across all the Cases was found to be approximately 250 to 260 HVn, which is notably within ranges experimentally determined by [101,102]. While hardness prediction is not a primary goal of this work, the similarity between the predicted and experimentally determined hardness supports the validity of the demonstrated modeling framework. The calculated hardness, however, may contain as much as ~23.57% uncertainty considering the mesh resolution of 10 μm on the surface of the subset, limiting the degree of accuracy when measuring the diagonals.

5. Conclusions

This paper parametrically examines the influence of microstructure modeling, inherent residual stress mapping, and environment temperature on the induced residual stress, during a hybrid metal-additive process, wherein interlayer burnishing is introduced in a selective laser melting setup. In the past, researchers have discussed changes in microstructure resulting from similar hybrid metal-additive processes, however, it was only hypothesized that the resulting microstructure may have some influence on the final state of induced residual stress. In addition, researchers have numerically investigated the influence of burnishing or rolling process parameters on induced stress but neglected the physical effects of microstructure, thereby assuming a homogeneous, isotropic material definition. Such practice inhibits the prediction of microstructure-driven anisotropy that can exist in the inhomogeneous fused layer. The demonstrated modeling framework incorporates an inherent residual stress field that emerges from the laser powder bed fusion process as well as the predicted microstructure, in a subsequent burnishing process to elucidate their influence on burnishing induced residual stress. Several important points and key findings appear from the demonstrated work.

This work represents the first study in which both the microstructure and residual stress from the laser powder bed fusion process are incorporated in a modeling framework to predict the residual stress field that evolves during an interlayer roller-burnishing process. The framework offers important insights into the decoupled influences of microstructure and SLM residual stress on burnishing-induced stresses that are not distinguishable via existing experimental techniques.

Incorporation of the inhomogeneous microstructure from the laser powder bed fusion process results in a non-uniform equivalent plastic strain response along the burnished surface. An equivalent plastic strain periodicity is revealed following burnishing, which is consistent with the spacing between successive scan lines from the laser powder bed fusion process. The corresponding peaks in the post-burnishing equivalent plastic strain are found to align with regions of the fused powder layer wherein fine, relatively equiaxed grains form, creating bands of high density of grain boundaries.

Modeling of the inhomogeneous microstructure obtained from laser powder bed fusion reveals its significant influence on both the surface and at-depth residual stresses that evolve during roller burnishing. In addition, residual stresses inherited from the powder bed fusion are less influential on the post-burnishing residual stresses, although their effects are not insignificant. The predicted trends in post-burnishing compressive residual stress in the rolling and axial directions, beneath the burnished surface, exhibit very similar trends to those documented in the literature using X-ray diffraction.

While elevated (warm) environment temperatures reduce the required burnishing loads when generating similar equivalent plastic strains, the corresponding magnitudes of induced compressive residual stress are found to be lower in general. The elevated temperatures promote grain boundary sliding amongst the fine grains, which form along the laser scan lines, resulting in less variation in residual stress predicted between the scan lines and the hatch spaces.

Declaration of competing interest

The authors declare that they have no known competing financial interests or personal relationships that could have appeared to influence the work reported in this paper.

Acknowledgment

Authors acknowledge the support of NSF CMMI-1762722. Any opinions, findings, or conclusions expressed in this paper are those of the authors and do not necessarily reflect the views of the U.S. National Science Foundation.

References

- Sartkulvanich P, Altan T, Jasso F, Rodriguez C. Finite element modeling of hard roller burnishing: an analysis on the effects of process parameters upon surface finish and residual stresses. 2007.
- [2] Sequera A, Fu C, Guo Y, Wei X. Surface integrity of Inconel 718 by ball burnishing. J Mater Eng Perform 2014;23(9):3347–53.
- [3] Manufacturing-Design-Part A. 1: Laser-based powder bed fusion of metals. 2019.
- [4] Moroni G, Petrò S, Shao H. On standardization efforts for additive manufacturing. In: Proceedings of 5th international conference on the industry 4.0 model for advanced manufacturing. Springer; 2020, p. 156–72.
- [5] Kalentics N, Boillat E, Peyre P, Ćirić-Kostić S, Bogojević N, Logé RE. Tailoring residual stress profile of selective laser melted parts by laser shock peening. Addit Manuf 2017:16:90–7.
- [6] Wang Z, Denlinger E, Michaleris P, Stoica AD, Ma D, Beese AM. Residual stress mapping in Inconel 625 fabricated through additive manufacturing: Method for neutron diffraction measurements to validate thermomechanical model predictions. Mater Des 2017;113:169–77.
- [7] Kalentics N, Boillat E, Peyre P, Gorny C, Kenel C, Leinenbach C, et al. 3D Laser Shock Peening-A new method for the 3D control of residual stresses in Selective Laser Melting. Mater Des 2017;130:350-6.
- [8] Kalentics N, Sohrabi N, Tabasi HG, Griffiths S, Jhabvala J, Leinenbach C, et al. Healing cracks in selective laser melting by 3D laser shock peening. Addit Manuf 2019:30:100881.
- [9] Meyer D, Wielki N. Internal reinforced domains by intermediate deep rolling in additive manufacturing. CIRP Ann 2019;68(1):579–82.
- [10] DebRoy T, Wei H, Zuback J, Mukherjee T, Elmer J, Milewski J, et al. Additive manufacturing of metallic components-process, structure and properties. Prog Mater Sci 2018;92:112–224.
- [11] Courbon C, Sova A, Valiorgue F, Pascal H, Sijobert J, Kermouche G, et al. Near surface transformations of stainless steel cold spray and laser cladding deposits after turning and ball-burnishing. Surf Coat Technol 2019;371:235–44.
- [12] Colegrove PA, Coules HE, Fairman J, Martina F, Kashoob T, Mamash H, et al. Microstructure and residual stress improvement in wire and arc additively manufactured parts through high-pressure rolling. J Mater Process Technol 2013;213(10):1782–91.
- [13] Donoghue J, Antonysamy A, Martina F, Colegrove PA, Williams SW, Prangnell P. The effectiveness of combining rolling deformation with Wire–Arc Additive Manufacture on β-grain refinement and texture modification in Ti–6Al–4V. Mater Charact 2016;114:103–14.
- [14] Zhou X, Zhang H, Wang G, Bai X, Fu Y, Zhao J. Simulation of microstructure evolution during hybrid deposition and micro-rolling process. J Mater Sci 2016;51(14):6735–49.
- [15] Colegrove PA, Martina F, Roy MJ, Szost BA, Terzi S, Williams SW, et al. High pressure interpass rolling of wire+ arc additively manufactured titanium components. In: Advanced materials research. vol. 996, Trans Tech Publ; 2014, p. 694–700.
- [16] Martina F, Roy M, Colegrove P, Williams S. Residual stress reduction in high pressure interpass rolled wire+ arc additive manufacturing Ti-6Al-4V components. In: Proc. 25th int. solid freeform fabrication symp. 2014, p. 89–94.
- [17] Fu Y, Zhang H, Wang G, Wang H. Investigation of mechanical properties for hybrid deposition and micro-rolling of bainite steel. J Mater Process Technol 2017;250:220–7.
- [18] Wang Z, Xiao Z, Huang C, Wen L, Zhang W. Influence of ultrasonic surface rolling on microstructure and wear behavior of selective laser melted Ti-6Al-4V alloy. Materials 2017;10(10):1203.

- [19] Breidenstein B, Brenne F, Wu L, Niendorf T, Denkena B. Effect of post-process machining on surface properties of additively manufactured H13 tool steel. HTM J Heat Treat Mater 2018;73(4):173–86.
- [20] Teramachi A, Yan J. Improving the surface integrity of additive-manufactured metal parts by ultrasonic vibration-assisted burnishing. J Micro Nano-Manuf 2019;7(2).
- [21] Ituarte InF, Salmi M, Papula S, Huuki J, Hemming B, Coatanea E, et al. Surface modification of additively manufactured 18% nickel maraging steel by ultrasonic vibration-assisted ball burnishing. J Manuf Sci Eng 2020;142(7).
- [22] Rotella G, Filice L, Micari F. Improving surface integrity of additively manufactured GP1 stainless steel by roller burnishing. CIRP Ann 2020.
- [23] Sunny S, Gleason G, Mathews R, Malik A. Simulation of laser impact welding for dissimilar additively manufactured foils considering influence of inhomogeneous microstructure. Mater Des 2020;109372.
- [24] Ahmad M, Akhter J, Shahzad M, Akhter M. Cracking during solidification of diffusion bonded Inconel 625 in the presence of Zircaloy-4 interlayer. J Alloys Compd 2008;457(1–2):131–4.
- [25] Dinda G, Dasgupta A, Mazumder J. Laser aided direct metal deposition of Inconel 625 superalloy: Microstructural evolution and thermal stability. Mater Sci Eng A 2009;509(1–2):98–104.
- [26] Li D, Guo Q, Guo S, Peng H, Wu Z. The microstructure evolution and nucleation mechanisms of dynamic recrystallization in hot-deformed Inconel 625 superalloy. Mater Des 2011;32(2):696–705.
- [27] Cai D, Xiong L, Liu W, Sun G, Yao M. Characterization of hot deformation behavior of a Ni-base superalloy using processing map. Mater Des 2009;30(3):921–5.
- [28] Handbook M. Properties and selection: nonferrous alloys and special-purpose materials. vol. 2, 1990, p. 713.
- [29] Michaleris P. Modeling metal deposition in heat transfer analyses of additive manufacturing processes. Finite Elem Anal Des 2014;86:51–60.
- [30] Lundbäck A, Lindgren L-E. Modelling of metal deposition. Finite Elem Anal Des 2011;47(10):1169–77.
- [31] Shrestha S, Starr T, Chou K. A study of keyhole porosity in selective laser melting: single-track scanning with micro-CT analysis. J Manuf Sci Eng 2019:141(7).
- [32] Shrestha S, Kevin Chou Y. A numerical study on the keyhole formation during laser powder bed fusion process. J Manuf Sci Eng 2019;141(10).
- [33] Tang M, Pistorius PC, Beuth JL. Prediction of lack-of-fusion porosity for powder bed fusion. Addit Manuf 2017;14:39–48.
- [34] Heigel JC, Lane BM. Measurement of the melt pool length during single scan tracks in a commercial laser powder bed fusion process. J Manuf Sci Eng 2018;140(5).
- [35] Moylan S, Whitenton E, Lane B, Slotwinski J. Infrared thermography for laser-based powder bed fusion additive manufacturing processes. In: AIP conference proceedings. vol. 1581, American Institute of Physics; 2014, p. 1191–6.
- [36] Lane B, Moylan S, Whitenton EP, Ma L. Thermographic measurements of the commercial laser powder bed fusion process at NIST. Rapid Prototyp J 2016.
- [37] Heigel JC, Lane BM. The effect of powder on cooling rate and melt pool length measurements using in situ thermographic techniques. In: Solid freeform fabrication symposium. 2017.
- [38] Short wave infrared camera dataset for ICR913 camera. 2020, https://ircameras.com/camera/irc912-swir/. [Accessed: 12 December 2020].
- [39] EOS M270 specifications EOS M270 specifications. 2020, http://www. 3rsystems.cz/en/3d-print/3d-print-dental/eosint-m270-metal. [Accessed: 12 December 2020].
- [40] NIST thermography dataset datasets for PBF-LB thermography from NIST on in625. 2020, https://www.nist.gov/el/lpbf-thermography/datasets. [Accessed: 24 November 2020].
- [41] Gouge M, Michaleris P. Thermo-mechanical modeling of additive manufacturing. Butterworth-Heinemann; 2017.
- [42] Chiumenti M, Cervera M, Salmi A, De Saracibar CA, Dialami N, Matsui K. Finite element modeling of multi-pass welding and shaped metal deposition processes. Comput Methods Appl Mech Eng 2010;199(37–40):2343–59.
- [43] Manvatkar V, Gokhale A, Reddy GJ, Venkataramana A, De A. Estimation of melt pool dimensions, thermal cycle, and hardness distribution in the laserengineered net shaping process of austenitic stainless steel. Metall Mater Trans A 2011;42(13):4080-7.
- [44] Denlinger ER, Gouge M, Irwin J, Michaleris P. Thermomechanical model development and in situ experimental validation of the Laser Powder-Bed Fusion process. Addit Manuf 2017;16:73–80.
- [45] Heigel J, Michaleris P, Reutzel EW. Thermo-mechanical model development and validation of directed energy deposition additive manufacturing of Ti-6Al-4V. Addit Manuf 2015:5:9-19.
- [46] Wei LC, Ehrlich LE, Powell-Palm MJ, Montgomery C, Beuth J, Malen JA. Thermal conductivity of metal powders for powder bed additive manufacturing. Addit Manuf 2018;21:201–8.
- [47] Foroozmehr A, Badrossamay M, Foroozmehr E, Golabi S. Finite element simulation of selective laser melting process considering optical penetration depth of laser in powder bed. Mater Des 2016;89:255–63.

- [48] Ali H, Ma L, Ghadbeigi H, Mumtaz K. In-situ residual stress reduction, martensitic decomposition and mechanical properties enhancement through high temperature powder bed pre-heating of Selective Laser Melted Ti6Al4V. Mater Sci Eng A 2017:695:211-20.
- [49] Lee Y, Zhang W. Mesoscopic simulation of heat transfer and fluid flow in laser powder bed additive manufacturing. In: International solid free form fabrication symposium. 2015, p. 1154–65.
- [50] Khairallah SA, Anderson AT, Rubenchik A, King WE. Laser powder-bed fusion additive manufacturing: Physics of complex melt flow and formation mechanisms of pores, spatter, and denudation zones. Acta Mater 2016;108:36–45.
- [51] Khairallah SA, Anderson A. Mesoscopic simulation model of selective laser melting of stainless steel powder. J Mater Process Technol 2014;214(11):2627– 36.
- [52] Li C, Denlinger ER, Gouge MF, Irwin JE, Michaleris P. Numerical verification of an octree mesh coarsening strategy for simulating additive manufacturing processes. Addit Manuf 2019;30:100903.
- [53] Sunny S, Yu H, Mathews R, Malik A, Li W. Improved grain structure prediction in metal additive manufacturing using a Dynamic Kinetic Monte Carlo framework. Addit Manuf 2020;101649.
- [54] Rodgers TM, Madison JD, Tikare V. Simulation of metal additive manufacturing microstructures using kinetic Monte Carlo. Comput Mater Sci 2017;135:78–89.
- [55] Garcia AL, Tikare V, Holm EA. Three-dimensional simulation of grain growth in a thermal gradient with non-uniform grain boundary mobility. Scr Mater 2008;59(6):661-4.
- [56] Olmsted DL, Foiles SM, Holm EA. Survey of computed grain boundary properties in face-centered cubic metals: I. Grain boundary energy. Acta Mater 2009;57(13):3694–703.
- [57] Gandin C-A, Desbiolles J-L, Rappaz M, Thevoz P. A three-dimensional cellular automation-finite element model for the prediction of solidification grain structures. Metall Mater Trans A 1999;30(12):3153–65.
- [58] Zinoviev A, Zinovieva O, Ploshikhin V, Romanova V, Balokhonov R. Evolution of grain structure during laser additive manufacturing. Simulation by a cellular automata method. Mater Des 2016;106:321–9.
- [59] Rai A, Markl M, Körner C. A coupled Cellular Automaton—Lattice Boltzmann model for grain structure simulation during additive manufacturing. Comput Mater Sci 2016;124:37–48.
- [60] Plimpton S, Thompson A, Slepoy A. Stochastic parallel PARticle kinetic simulator. Technical report, Sandia National Laboratories; 2008.
- [61] Li S, Wei Q, Shi Y, Zhu Z, Zhang D. Microstructure characteristics of Inconel 625 superalloy manufactured by selective laser melting. J Mater Sci Technol 2015;31(9):946–52.
- [62] Ganesh P, Kaul R, Paul C, Tiwari P, Rai S, Prasad R, et al. Fatigue and fracture toughness characteristics of laser rapid manufactured Inconel 625 structures. Mater Sci Eng A 2010;527(29–30):7490–7.
- [63] Pleass C, Jothi S. Influence of powder characteristics and additive manufacturing process parameters on the microstructure and mechanical behaviour of Inconel 625 fabricated by Selective Laser Melting. Addit Manuf 2018;24:419–31.
- [64] Li C, White R, Fang X, Weaver M, Guo Y. Microstructure evolution characteristics of Inconel 625 alloy from selective laser melting to heat treatment. Mater Sci Eng A 2017;705:20–31.
- [65] Serrano-Munoz I, Fritsch T, Mishurova T, Trofimov A, Apel D, Ulbricht A, et al. On the interplay of microstructure and residual stress in LPBF IN718. J Mater Sci 2021;56(9):5845–67.
- [66] Li C, Guo Y, Zhao J. Interfacial phenomena and characteristics between the deposited material and substrate in selective laser melting Inconel 625. J Mater Process Technol 2017;243:269–81.
- [67] Koutiri I, Pessard E, Peyre P, Amlou O, De Terris T. Influence of SLM process parameters on the surface finish, porosity rate and fatigue behavior of as-built Inconel 625 parts. J Mater Process Technol 2018;255:536–46.
- [68] Yan X, Gao S, Chang C, Huang J, Khanlari K, Dong D, et al. Effect of building directions on the surface roughness, microstructure, and tribological properties of selective laser melted Inconel 625. J Mater Process Technol 2021;288:116878.
- [69] Dunbar A, Denlinger E, Heigel J, Michaleris P, Guerrier P, Martukanitz R, et al. Development of experimental method for in situ distortion and temperature measurements during the laser powder bed fusion additive manufacturing process. Addit Manuf 2016;12:25–30.
- [70] Sibson R. A brief description of natural neighbour interpolation. John Wiley & Sons; 1981.
- [71] Musashi JP, Pramoedyo H, Fitriani R. Comparison of inverse distance weighted and natural neighbor interpolation method at air temperature data in Malang Region. Cauchy 2018;5(2):48–54.
- [72] Belikov V, Ivanov V, Kontorovich V, Korytnik S, Semenov AY. The non-sibsonian interpolation: A new method of interpolation of the value of a function on an arbitrary set of points. Zh Vychisl Mat Mat Fiz 1997;37(1):11–7.
- [73] Renz A, Khader I, Kailer A. Tribochemical wear of cutting-tool ceramics in sliding contact against a nickel-base alloy. J Eur Ceram Soc 2016;36(3):705–17.

- [74] Johnson GR, Cook WH. A constitutive model and data for metals subjected to large strains, high strain rates and high temperatures. In: Proceedings of the 7th international symposium on ballistics. vol. 21, The Netherlands; 1983, p. 541–7
- [75] Hall E. The deformation and ageing of mild steel: III discussion of results. Proc Phys Soc Sect B 1951;64(9):747.
- [76] Petch N. The cleavage strength of polycrystals. J Iron Steel Inst 1953;174:25-8.
- [77] Lindgren L-E, Lundbäck A, Fisk M, Pederson R, Andersson J. Simulation of additive manufacturing using coupled constitutive and microstructure models. Addit Manuf 2016:12:144–58.
- [78] Wang Z, Palmer TA, Beese AM. Effect of processing parameters on microstructure and tensile properties of austenitic stainless steel 304L made by directed energy deposition additive manufacturing. Acta Mater 2016;110:226–35.
- [79] Hokka M, Gomon D, Shrot A, Leemet T, Bäker M, Kuokkala V-T. Dynamic behavior and high speed machining of ti-6246 and alloy 625 superalloys: experimental and modeling approaches. Exp Mech 2014;54(2):199–210.
- [80] Lotfi M, Jahanbakhsh M, Farid AA. Wear estimation of ceramic and coated carbide tools in turning of Inconel 625: 3D FE analysis. Tribol Int 2016;99:107–16.
- [81] Gao Y, Zhou M. Superior mechanical behavior and fretting wear resistance of 3D-printed Inconel 625 superalloy. Appl Sci 2018;8(12):2439.
- [82] John MS, Banerjee N, Shrivastava K, Vinayagam B. Optimization of roller burnishing process on EN-9 grade alloy steel using response surface methodology. J Braz Soc Mech Sci Eng 2017;39(8):3089–101.
- [83] Kang N, Ma W, Heraud L, El Mansori M, Li F, Liu M, et al. Selective laser melting of tungsten carbide reinforced maraging steel composite. Addit Manuf 2018;22:104-10.
- [84] Zhao W, Yang Q, Khan AM, He N, Zhang A. An inverse-identification-based finite element simulation of orthogonal cutting tungsten carbide. J Braz Soc Mech Sci Eng 2019;41(2):85.
- [85] Ku N, Pittari JJ, Kilczewski S, Kudzal A. Additive manufacturing of cemented tungsten carbide with a cobalt-free alloy binder by selective laser melting for high-hardness applications. Jom 2019;71(4):1535–42.
- [86] Deo M, Michaleris P. Mitigation of welding induced buckling distortion using transient thermal tensioning. Sci Technol Welding And Joining 2003;8(1):49–54.
- [87] Xie P, Zhao H-Y, Wu B, Gong S-L. Using finite element and contour method to evaluate residual stress in thick Ti-6Al-4V alloy welded by electron beam welding. Acta Metall Sin Engl Lett 2015;28(7):922–30.

- [88] De Oliveira MM, Couto AA, Almeida GF, Reis DA, De Lima NB, Baldan R. Mechanical behavior of Inconel 625 at elevated temperatures. Metals 2019;9(3):301.
- [89] Ziaja W, Motyka M, Poręba M. Plasticity of nickel-based superalloy 625 at elevated temperature. Adv Manuf Sci Technol 2017;41(4).
- [90] Guo Q, Li D, Guo S, Peng H, Hu J. The effect of deformation temperature on the microstructure evolution of Inconel 625 superalloy. J Nucl Mater 2011;414(3):440–50.
- [91] Hu Y, Lin X, Li Y, Zhang S, Gao X, Liu F, et al. Plastic deformation behavior and dynamic recrystallization of Inconel 625 superalloy fabricated by directed energy deposition. Mater Des 2020;186:108359.
- [92] Nordström J, Siriki R, Moverare J, Chai G. Deformation twinning behavior in high Ni-austenitic materials. In: Materials science forum. vol. 941, Trans Tech Publ; 2018, p. 1591–6.
- [93] Gao Y, Ding Y, Chen J, Xu J, Ma Y, Wang X. Effect of twin boundaries on the microstructure and mechanical properties of Inconel 625 alloy. Mater Sci Eng A 2019;767:138361.
- [94] Liu F, Nelson T. Grain structure evolution, grain boundary sliding and material flow resistance in friction welding of Alloy 718. Mater Sci Eng A 2018;710:280–8.
- [95] Liu F, Xue P, Ma Z. Microstructural evolution in recrystallized and unrecrystallized Al–Mg–Sc alloys during superplastic deformation. Mater Sci Eng A 2012;547:55–63.
- [96] Sridhar B, Devananda G, Ramachandra K, Bhat R. Effect of machining parameters and heat treatment on the residual stress distribution in titanium alloy IMI-834. J Mater Process Technol 2003;139(1–3):628–34.
- [97] Juijerm P, Altenberger I. Effect of temperature on cyclic deformation behavior and residual stress relaxation of deep rolled under-aged aluminium alloy AA6110. Mater Sci Eng A 2007;452:475–82.
- [98] Chomienne V, Valiorgue F, Rech J, Verdu C. Influence of ball burnishing on residual stress profile of a 15-5PH stainless steel. CIRP J Manuf Sci Technol 2016;13:90–6.
- [99] Standard A. E384-17, Standard Test Method for Microindentation Hardness of Materials, pp. 1-40.
- [100] Herrmann K, et al. Hardness testing: principles and applications. ASM international; 2011.
- [101] Badiger RI, Narendranath S, Srinath M. Microstructure and mechanical properties of Inconel-625 welded joint developed through microwave hybrid heating. Proc Inst Mech Eng B 2018;232(14):2462–77.
- [102] Shakil M, Ahmad M, Tariq N, Hasan B, Akhter J, Ahmed E, et al. Microstructure and hardness studies of electron beam welded Inconel 625 and stainless steel 304L. Vacuum 2014:110:121–6.